Vestfold University College

Master Thesis

A study on RF MEMS switches using CuO dielectric

Author:
Bao Dang Ho

Supervisors:
Prof. Ulrik Hanke
Prof. Nils Høivik

A thesis submitted in fulfilment of the requirements for the degree of Master of Engineering

in the

Department of Micro and Nano Systems Technology

May 2013

"Iron rusts from disuse; water loses its purity from stagnation... even so does inaction sap the vigor of the mind."

Leonardo da Vinci

VESTFOLD UNIVERSITY COLLEGE

Abstract

Faculty of Technology and Maritime Sciences
Department of Micro and Nano Systems Technology

Master of Engineering

A study on RF MEMS switches using CuO dielectric

by Bao Dang Ho

This thesis is a continual work in the topic of RF MEMS switches which has been developed before at the Department of Micro and Nano System Technology. The work focuses on finding a high-k yet low-cost and easy to fabricate dielectric material for capacitive RF MEMS switch. It also studies on analysis and simulation of capacitive RF MEMS shunt switches to help design and optimize their dimensions so as to fit a specific application.

In experimental part, the thesis choose CuO to study and has found that it has a low dielectric strength of 0.2 MV/cm. When annealing CuO, dendrite structures emerging above the oxide surface have been observed and explained. In theoretical part, analysis and simulation of RF MEMS switches have been performed in both electromechanics and electromagnetism. It is found that besides bending, stretching effect and especially, residual stress have strong effect on mechanical behavior of the switches, particularly the pull-in voltage. Also, a new 2D mathematical model has been built to better study mechanical properties of RF MEMS switches.

Acknowledgements

I would first like to thank Prof. Ulrik Hanke and Prof. Nils Høivik for their guidance, comments, discussion and encouragement for me to accomplish this thesis. On every weekly group meeting, I have learned not only knowledge but also experience in doing lab work, presenting ideas, discussing problems and most importantly, how independent scientific work should be carried out.

I also would like to thank PhD Deokki Min for his help in RF measurement, for his useful discussion and comments. Next, I would like to thank IMST lab engineer Zekija Ramic for her helps in my various lab work, lab engineer Thomas Marthinsen and Ragnar Dahl Johansen for helping me with lab instruments, lab engineer Svein Mindrebøe for his help with the shadow mask. I also would like to thank Prof. Erik Johannessen, Assoc. Prof. Agne Johannessen and Prof. Knut E. Aasmundtveit for their helpful discussion and comments on my work.

I also would like to thank PhD candidates Anh Tuan Nguyen Thai, Duy Le, Van Khanh Nguyen for their direct help on my thesis.

Last but not least, special thanks to my family and my friends who are always behind and support me in following scientific work.

Contents

List of Figures

List of Tables

Abbreviations

RF	Radio frequency
CPW	Coplanar wave guide
MEMS	Micro electromechanical systems

To my beloved parents, who always encourage me to follow my own dream.

This page is intentionally left blank.

Chapter 1

Introduction

As its name suggests, RF MEMS switches are devices used to allow/stop transmission of high frequency electrical signal in RF applications, which can be found in satellites, antennas or cellular phones. The distinction between RF MEMS switches and other switches of the same purpose, like PIN diodes or FET switches, is the involvement of mechanical parts, fabricated using bulk or surface micromachining technology. This mechanical-driven mechanism bring outs excellent performance of RF MEMS switches over their competitors: virtually no power consumption, low insertion loss and high isolation. The history of RF MEMS switch dates back to the early 1990s when the first MEMS switch was fabricated at the Hughes Research Labs in Malibu, California by Lawrence E. Larson et al. [1]. Since then, this new approach has drawn attention of many reserch labs and electronic companies around the world [2] [3] [4] [5] [6] [7] [8] [9].

Observing the potential growth of RF MEMS switch, the Department of Micro and Nano Systems Technology at Vestfold University College has also made this a topic in its research activity. In 2011, microfabrication process for making electrostatically actuated, capacitive RF MEMS shunt switches was successfully developed by PhD Deokki Min et al. [10]. In that work, PZT/ZrO_2 thin film has also been deposited and characterized, being a potentially high dielectric constant material for making high isolation switch. The above promising results have raised interests and motivated the author to conduct a continual research in the topic of RF MEMS switch.

Since its existence, the traditional dielectric materials for capacitive RF MEMS switches are silicon oxide or silicon nitride, which have dielectric constants of about 4 and 6, respectively. These materials are well-known, have good mechanical properties and their deposition techniques are well-established. However, their limitation lies in their low

values of dielectric constants, which also means low capacitance ratio and difficulty in obtaining high RF isolation. Therefore, it is tempted to replace them by alternate dielectric materials that have significantly higher dielectric constant. *This is the first research problem of this thesis.* In general there are two groups of high dielectric constant materials: ferroelectrics and metal oxides. This thesis will focus on the latter and in-house physical techniques, thermal evaporation and thermal oxidation, are intended to use in depositing dielectric thin film. Those methods are chosen because they would help the fabrication process for making RF MEMS switch be done totally in-house at the Department's lab. If the first research question has an optimistic answer, there will appear a new generation of RF MEMS switch which have micro-scaled size, almost no DC power consumption, high capacitance ratio and high isolation in down-state. Furthermore, they are cheap and can be fabricated in-house at the IMST's lab.

After the process for fabrication of RF MEMS switch has been made available by Deokki, a question is naturally raised: can that process be used to make switches for an actual, specific RF application? *This is also the second research question of this thesis.* The answer for this question, together with the high-κ dielectric that could be found, would together build a framework for making new RF MEMS switches that are low-cost yet possess high capacitance ratio and high isolation.
To answer the second question thoroughly, cares should be taken. Firstly, important characteristics like pull-in voltage, switching time and RF isolation are dependent on material and geometry of the switches and that dependency should be studied to well design an application-oriented switch. Secondly, process parameters, such as residual stress and etching holes, could also affect the properties of the switch and in most cases their presence cannot be neglected. This thesis, by modeling, analysis and simulation, attempts to explore the effects of geometry, material properties and process parameters to characteristics of the switches and then propose a switch design that could be used in a specific application. The targeted application in this thesis is the switching networks, which are necessary in most communication systems, especially communication satellites. There are two advantages that make RF MEMS switches suitable for communication satellites application. First, these switches have much less power consumption than PIN diodes and thus, in satellites where power source is limited to solar cell, they are preferable to PIN diodes. Secondly, micromachined switches are small and light, making them potential replacements for the traditional coaxial switches used in satellite, which are much more heavier.

The thesis includes six chapters. Following this introductory chapter, chapter two provides background about RF MEMS, RF MEMS switches and necessary knowledge about

RF engineering, which will be applied later in chapter three. Chapter three, method, presents detailed work in electromechanical and electromagnetic analysis and simulation of RF MEMS switches. The final section of chapter three show the process of searching high-κ metal oxide dielectric for RF MEMS switch and then describes details in fabrication and characterization of a potential candidate, copper (II) oxide. Then comes chapter four with harvested results of what have been introduced in chapter three. Chapter five follows with discussion about the results in chapter four. Chapter six concludes the thesis and suggests future work. Some Matlab programs are shown in appendix for reference.

Chapter 2

Background

2.1 RF MEMS

RF MEMS is the acronym of Radio Frequency Microelectromechanical System(s), referring to any micromachined devices or parts which perform RF functionality. RF MEMS can also be used as an adjective, as in the phrase "RF MEMS switch", to describe that the device or part is an RF MEMS. According to [11, p. 2], research in the field of RF MEMS can be categorized into four main areas, summarized in Figure 2.1.

However in [12, p. 2], Stepan narrows down the range of systems which can be considered RF MEMS. According to this author point of view, true RF MEMS have reconfigurable actuators that is independent of input RF signal. Therefore, immovable RF MEMS inductors and antennas, RF micromechanical resonators and filters, and FBAR, which is excited by input RF signal, are not true RF MEMS. Nevertheless, the exact definition of RF MEMS is not a big concern of this thesis since its main focus is RF MEMS switches, which are definitely true RF MEMS.

2.2 RF MEMS switches

As the name suggests, RF MEMS switches are RF MEMS device that can allow or block RF current/power. Figure 2.2 and Figure 2.3 demonstrate an RF MEMS capacitive shunt switch in up-state position and down state position respectively. In the figures, the yellow color denotes gold coplanar wave guide and suspension bridge and the green color denotes a high-κ dielectric layer. The switch is called capacitive because the suspension bridge, the air and dielectric layer and the transmission line region below the bridge together form a capacitor. When the bridge is up, the up-state capacitance is

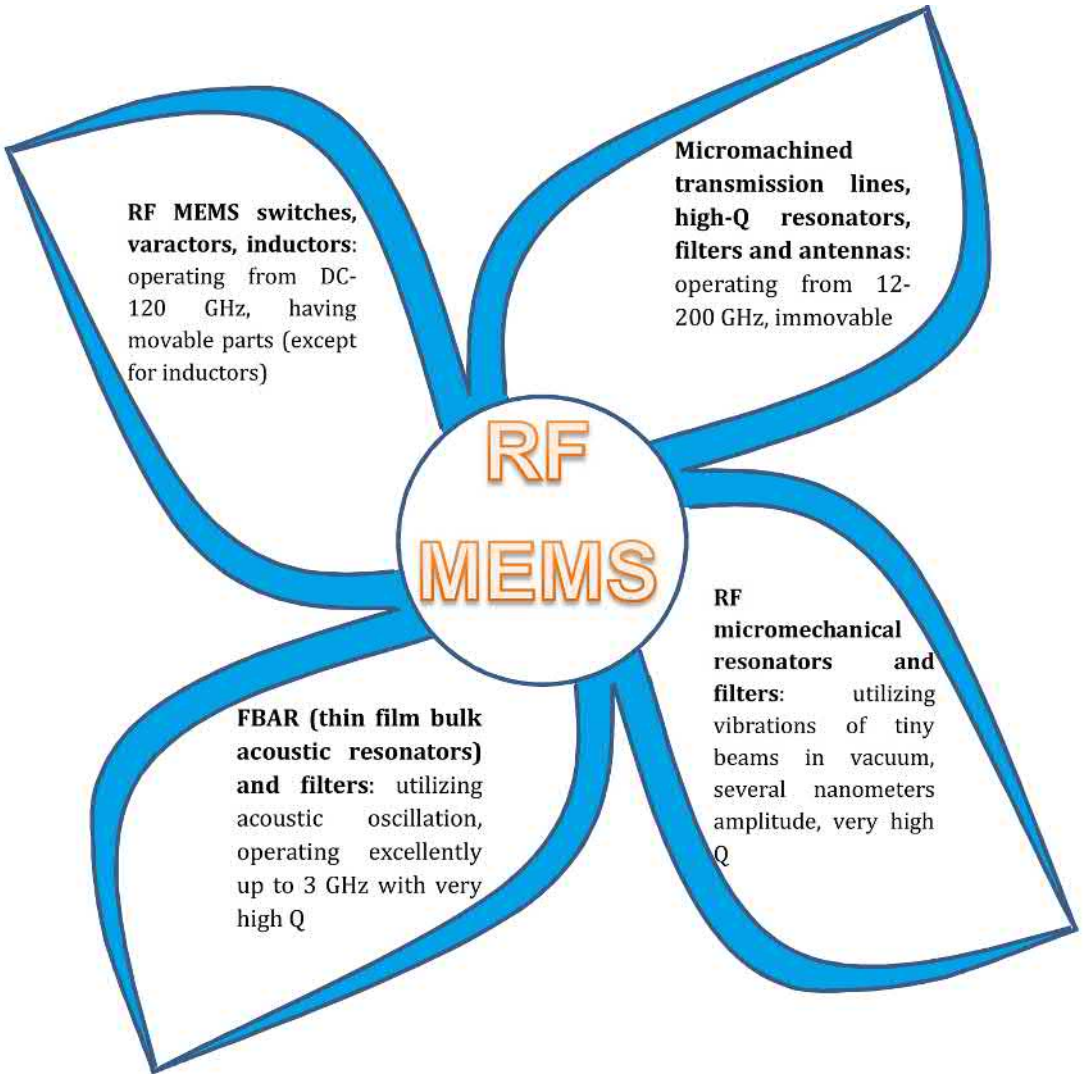

FIGURE 2.1: Main areas of RF MEMS research

low due to large distance and low dielectric constant of the air and thus, the switch has almost no effect on the RF current transmitted over the middle transmission line, the switch is in on-state. On the other hand, when the bridge is down, that the down state capacitance is large makes the switch impedance small. General speaking, the input RF signal is grounded and thus, the output signal is almost zero. More precisely, the input RF signal is reflected back to the source because the down-state switch form a discontinuity on the transmission line.

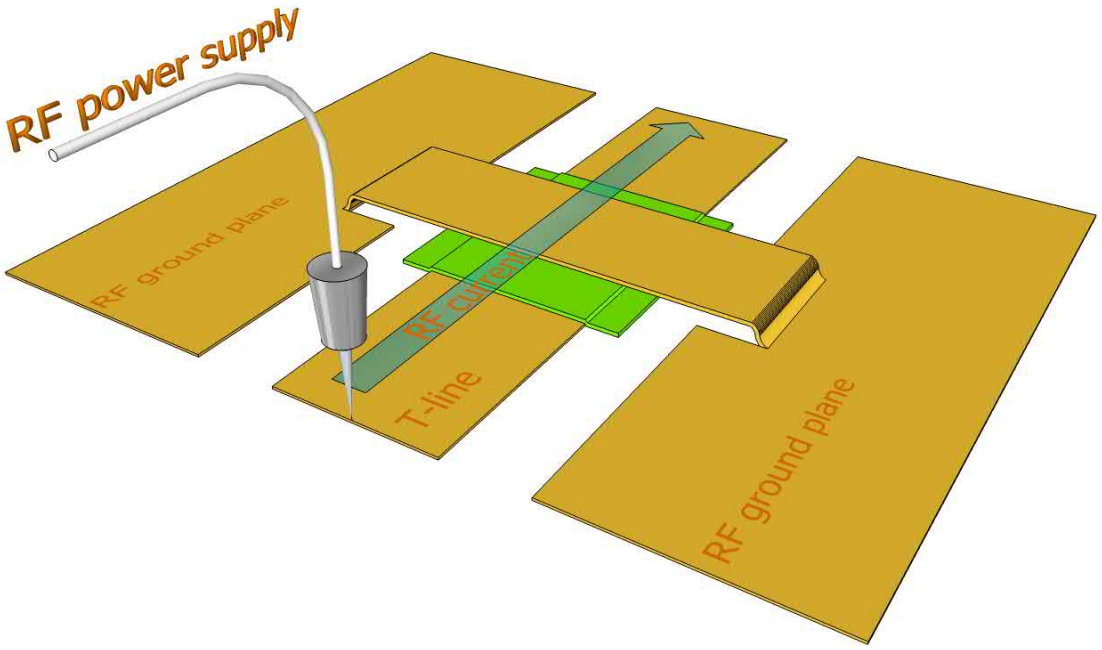

FIGURE 2.2: An RF MEMS capacitive shunt switch in up-state position

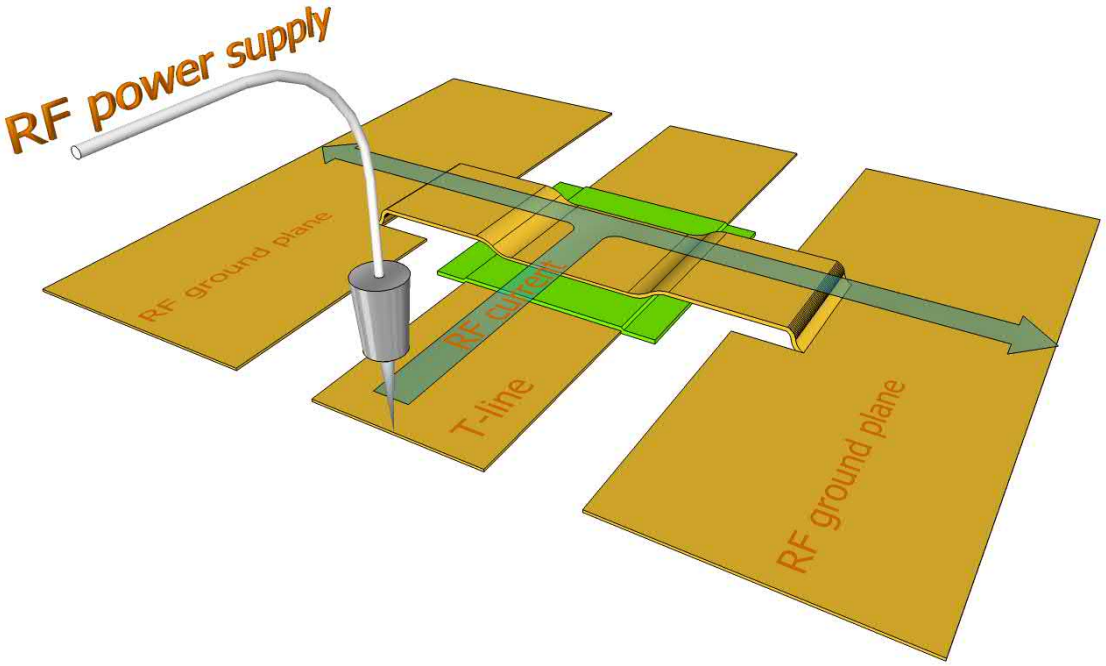

FIGURE 2.3: An RF MEMS capacitive shunt switch in down-state position

2.3 Some basic knowledge about RF engineering

2.3.1 Two-port network and s-parameters

A two-port network, in electrical engineering, is an electrical circuit or device which has two ports, usually one is considered input port and the other is thought as output port.

Each port consists of two terminals as depicted in figure 2.4

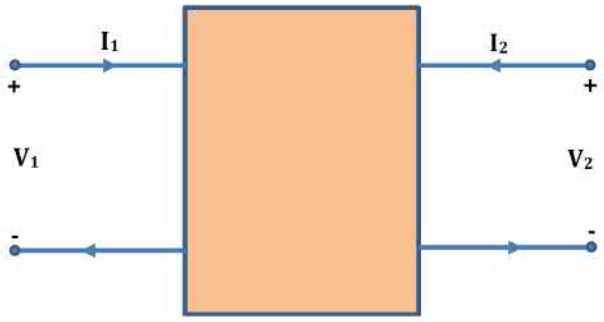

z-parameters

$$\begin{bmatrix} V_1 \\ V_2 \end{bmatrix} = \begin{bmatrix} z_{11} & z_{12} \\ z_{21} & z_{22} \end{bmatrix} \begin{bmatrix} I_1 \\ I_2 \end{bmatrix}$$

y-parameters

$$\begin{bmatrix} I_1 \\ I_2 \end{bmatrix} = \begin{bmatrix} y_{11} & y_{12} \\ y_{21} & y_{22} \end{bmatrix} \begin{bmatrix} V_1 \\ V_2 \end{bmatrix}$$

h-parameters

$$\begin{bmatrix} V_1 \\ I_2 \end{bmatrix} = \begin{bmatrix} h_{11} & h_{12} \\ h_{21} & h_{22} \end{bmatrix} \begin{bmatrix} I_1 \\ V_2 \end{bmatrix}$$

FIGURE 2.4: A two port network (above) and its z-parameters, y-parameters and h-parameters (below)

In DC or low-frequency electrical engineering, the wave length of electromagnetic wave transmitted in a circuit is much larger than dimensions of the circuit itself; thus, current and voltage are considered to be the same over, for example, a transmission line in the circuit. As a result, a two-port network in DC and low-frequency electrical engineering is usually modelled by sets of parameters that describe relationships between the values of voltage or current of input and output port, for example, impedance parameters (z-parameters), admittance parameters (y-parameters), hybrid parameters (h-parameters) as depicted in figure 2.4.

However, the z, y and h-parameters are no longer applicable for a two-port network under high-frequency excitations. The first reason is that in order to calculate these parameters, short circuit or open circuit condition has to be implemented on a certain port, which is difficult for RF signal because of lead inductance and capacitance. Secondly, for high-frequency signals having wavelength in sub-meter range, the circuit dimensions are comparable to the signal wavelength. Therefore, voltage and current are not the same over a transmission line but depend on position relative to the source. As a result, a new set of parameters that can better describe the scattering nature of the RF signal, called scattering parameters (s-parameters), is defined. In order to calculate s-parameters, new variables called wave variables are introduced: a_1, a_2 are waves travelling into port 1 and port 2 respectively and b_1, b_2 are waves travelling out of port 1 and port 2 respectively. These wave variables can be defined by voltages and currents at the two ports and a real-valued positive reference impedance Z_0 (ususally chosen to

be 50Ω), as shown in equation 2.1. These wave variables are complex numbers, which means they have both amplitude and phase. Physically, $|a_1|^2$ is the maximum power that the source having source impedance Z_0 can supply to the two-port network, $|b_1|^2$ is the power that reflected back from the two-port network and $|a_1|^2 - |b_1|^2$ is the actual power that the two-port network receive from the source [13].

$$a_1 = \frac{V_1 + I_1 Z_0}{2\sqrt{Z_0}},\ b_1 = \frac{V_1 - I_1 Z_0}{2\sqrt{Z_0}}, \qquad a_2 = \frac{V_2 + I_2 Z_0}{2\sqrt{Z_0}},\ b_2 = \frac{V_2 - I_2 Z_0}{2\sqrt{Z_0}} \tag{2.1}$$

The s-parameters can then be defined based on aforementioned wave variables:

$$\begin{bmatrix} b_1 \\ b_2 \end{bmatrix} = \begin{bmatrix} s_{11} & s_{12} \\ s_{21} & s_{22} \end{bmatrix} \begin{bmatrix} a_1 \\ a_2 \end{bmatrix} \tag{2.2}$$

where usually, s_{11}, s_{22} are called input reflection coefficient, output reflection coefficient, respectively and s_{21}, s_{12} are called forward transmission coefficient, reverse transmission coefficient, respectively.

To illustrate, let consider a two-port network that connected with source and load by two transmission line having characteristic impedance Z_0 as shown in figure 2.5.

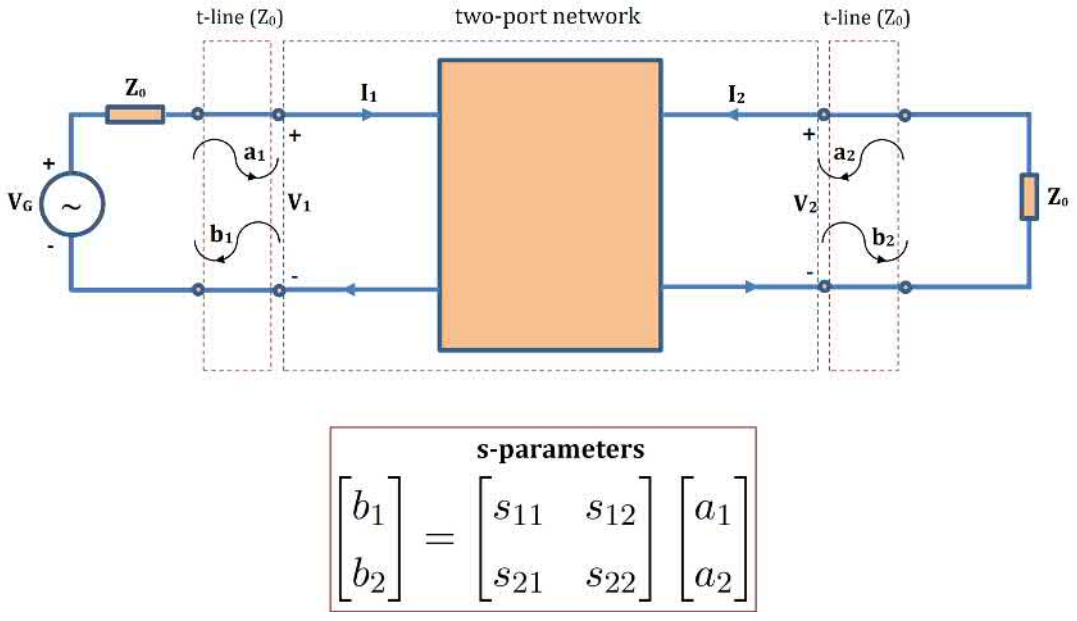

FIGURE 2.5: A two port network and its s-parameters

The source and the load have the same impedance Z_0. The incident wave a_1 travelling into port 1 will be partially transmitted throuth the two-port network to port 2 (b_2) and partially reflected back towards the source (b_1). If the load impedance $Z_L \neq Z_0$, then

there will be reflected wave from the load a_2. However, since the load impedance is the same as the characteristic impedance of the transmission line, b_2 is totally absorbed and $a_2 = 0$ (the reader may find explanation for this in [14, p. 56]). From equation 2.2 with a_2 set to zero, one can find s_{11} and s_{21}. With similar practice, s_{22} and s_{12} can also be found. Equation 2.3 illustrates these calculations.

$$\begin{aligned} s_{11} &= \frac{b_1}{a_1} \mid_{a_2=0} \\ s_{21} &= \frac{b_2}{a_1} \mid_{a_2=0} \\ s_{22} &= \frac{b_2}{a_2} \mid_{a_1=0} \\ s_{12} &= \frac{b_1}{a_2} \mid_{a_1=0} \end{aligned} \tag{2.3}$$

Chapter 3

Method

3.1 Electromechanical analysis and simulation of RF MEMS switches

This section presents the method for electromechanical analysis and simulation of RF MEM switches. Mathematical analysis explores which parameters can affect the behavior of the switches and how strong the dependency is. For example, it can find out which dimensions or material properties would lower the pull in voltage and switching time of the switch and further more, which is the most dominant factor. However, analysis work usually makes assumptions to simplify, for example the differential equations to be solved, and thus yields approximate solution. Numerical simulation, on the other hand, can give solution just in cases where all parameters have predefined values, nevertheless the results obtained are precise given that the mesh and boundary conditions are well defined. Since analysis or simulation work has its own advantages and can support each other in modelling RF MEMS switches, both of them are focused in this section.

In simple analysis, the switch is usually modeled as a fixed-fixed beam with only pure bending and is actuated by a DC biased voltage at the central region. Furthermore, the central part of the switch and the bottom electrode form a perfect parallel-plate capacitor. However in many cases, these assumptions are inefficient to yield precise solution to the deflection and pull-in voltage of the switch. Some additional contributions should be taken into account to better analyze the switch:

- *Electrical fringing field* originates from the edges and (much smaller) from the back side of the bridge and the bottom electrode. Neglecting fringing effect can lead to underestimating the electrostatic force between the bridge and the bottom electrode.

- *Axial stress* presents due to stretching of the bridge. The stiffness comes from stretching can be comparable to that originates from bending when the bridge deflects a distance as large as its thickness.
- *Residual stress* is induced from fabrication process. For example, when using evaporator to deposit the bridge of a shunt switch, the temperature in evaporation process is usually higher than the working temperature of the switch, which may introduce compressive stress in the switch.
- *Etching holes* are designed to promote etching and release process. These holes may alter the stiffness and air damping of the bridge.

This section presents methods to analyze the above effects on electromechanical properties of RF MEMS switches. Dimensions and data of the modeled switches are shown in Figure 3.1 and Table 3.1.

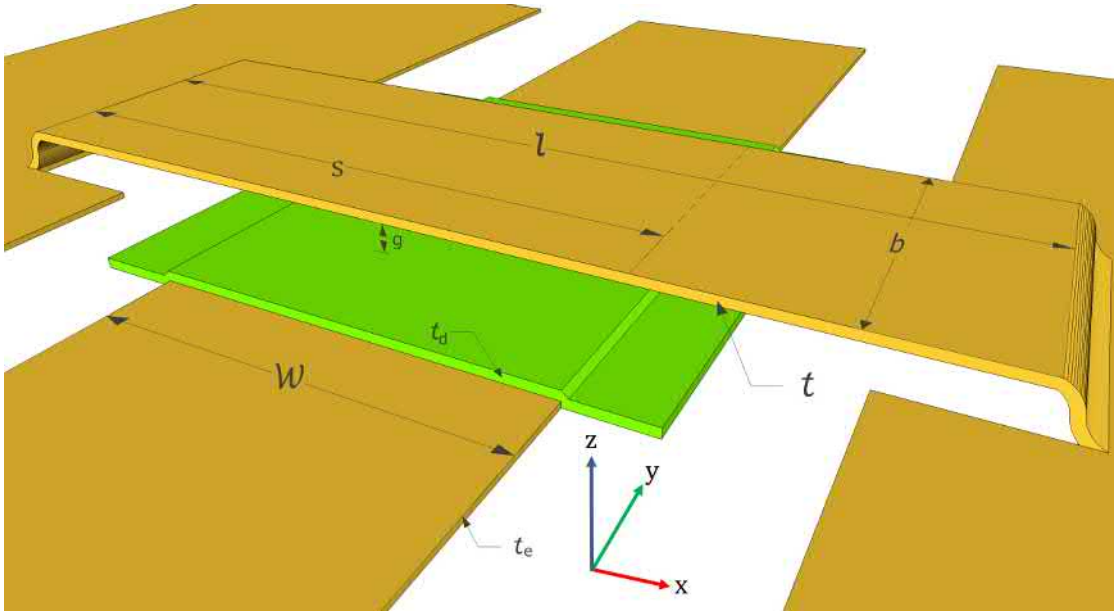

FIGURE 3.1: Geometry of the modeled switch (etching holes are not drawn)

3.1.1 Fringing field effect

Electrical fringing field originating from the edges, the back side of the bridge and the bottom electrode increases the capacitance and the electrical force acting on the bridge. The emperical formula of van de Meijs and Fokkema [15], among others, is suitable for analyzing fringing field effect in RF MEMS switch because it is simpler than other formulas like [16] but still yields accurate results in a wide range of dimensions. The formula is applied for a long bridge of thickness t and width w, suspended at distance h over a ground plane as can be seen in Figure 3.2.

TABLE 3.1: Data of the modeled switch

Name	Notation	Value
Young modulus of gold	E_{Au}	$70\ GPa$
Poisson ration of gold	ν	0.44
Displacement in x, y, z directions	$u,\ v,\ w$	
Initial air gap	g_0	$0.5,\ 1,\ 2\ \mu m$
Air gap	g	$g_0 - w$
Thickness of dielectric layer	t_d	$0.5,\ 0.2 - 0.3\ \mu m$
Relative dielectric constant of copper oxide	ε_r	18.1
Dielectric constant of vacuum	ε_0	$8.85 \times 10^{-12}\ F/m$
Effective initial air gap	g_{eff0}	$g_0 + t_d/\varepsilon_r$
Effective air gap	g_{eff}	$g_{eff0} - w$
Bridge length	l	$280\ \mu m$
Bridge width	b	$40,\ 60,\ 80\ \mu m$
Bridge thickness	t	$0.5,\ 1,\ 2\ \mu m$
Thickness of bottom electrode	t_e	$0.5\ \mu m$
Width of bottom electrode	W	$100\ \mu m$
Distance from one end of the bridge to a boundary of central region (see Figure)	s	$(l + W)/2$
Axial residual stress	T_0	$10,\ 20,\ 30\ MPa$
Diameter of etching holes	d_{hole}	$3.75\ \mu m$
Hole pitch (distance between two holes)	$pitch$	$6.25\ \mu m$

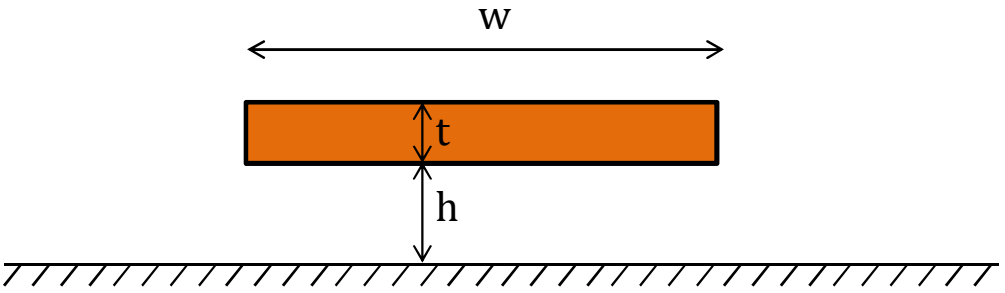

FIGURE 3.2: A conductor plate over ground plane

Van de Meijs and Fokkema claimed that for $w/h \geq 1$ and $0.1 \leq t/h \leq 4$, the following formula approximates well exact formula within 2% accuracy:

$$\frac{C}{\varepsilon_0 \varepsilon_r} = \frac{w}{h} + 0.77 + 1.06 \left(\frac{w}{h}\right)^{0.25} + 1.06 \left(\frac{t}{h}\right)^{0.5} \tag{3.1}$$

One can see that the total capacitance includes the parallel-plate capacitance, a constant term, one term depended on the w/h ratio and one term depended on the t/h ratio.

To apply equation 3.1 in RF MEMS switch, let us consider a simplified model shown in Figure 3.3, where the arrows symbolically denote the fringing electrical field. The bridge is made partially transparent for a better view.

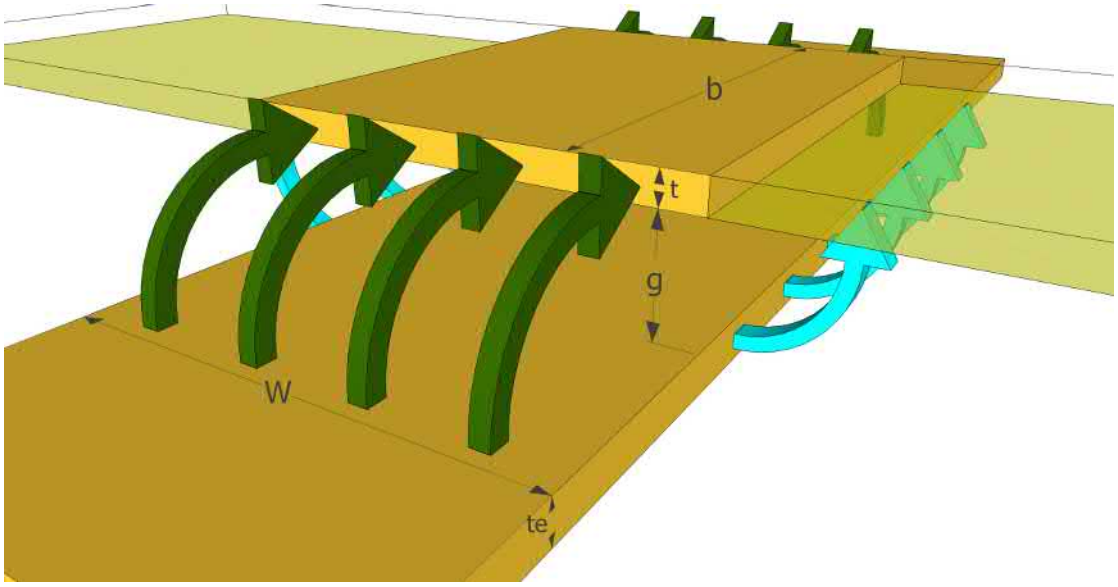

FIGURE 3.3: Model to study fringing field effect in RF MEMS switch

Since the bridge and the bottom electrode span across each other, there are two fringing contributions to the total capacitance: the dark green field and the light blue field in Figure 3.3. Applying Equation 3.1, the capacitance of the model shown in Figure 3.3 is:

$$\frac{C}{\varepsilon_0} = \frac{bW}{g} + 0.77(b+W) + 1.06W\left(\frac{t}{g}\right)^{0.5} + 1.06b\left(\frac{t_e}{g}\right)^{0.5} + 1.06(b^{0.75}+W^{0.75})\left(\frac{bW}{g}\right)^{0.25} \tag{3.2}$$

The electrostatic force can be derived from the total capacitance:

$$\begin{aligned} F_e &= -\frac{1}{2}V^2\frac{\partial C}{\partial g} \\ &= \frac{\varepsilon_0 bWV^2}{2g^2}\left[1 + \frac{0.53}{b}(tg)^{0.5} + \frac{0.53}{W}(t_e g)^{0.5} + 0.265g^{0.75}\frac{b^{0.75}+W^{0.75}}{(bW)^{0.75}}\right] \end{aligned} \tag{3.3}$$

It can be seen that the first term in Equation 3.2 and Equation 3.3 accounts for the parallel-plate capacitance and force, whereas the other terms account for fringing effect. When applying the above formulas, due to the presence of the dielectric layer the effective gap should be use instead of only the air gap.

3.1.2 Derivation of spring constant component due to bending

We model the bridge as a rectangular plate clamped at two opposite boundaries and free at remaining boundaries. The plate has length l, width b, thickness t and is loaded with uniform pressure q at the center portion of dimensions $b \times W$ (see Figure 3.4). For later convenience, the coordinates are denoted as X and Y instead of x and y as usual. The variables $x,\ y$ are used to denote the normalized values of $X,\ Y$ to the length of the bridge.

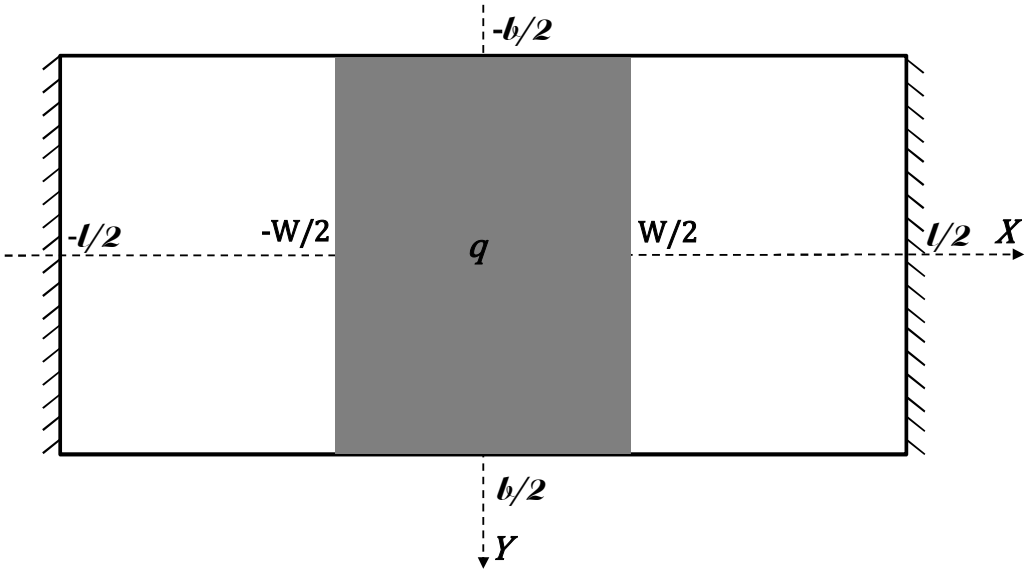

FIGURE 3.4: 2D model of RF MEMS switch

Assuming that $t << l$ and $t << b$, which is usually the case, and the plate moves a distance smaller than its thickness t so that we can neglect stretching of the plate for now.

A. 1D analysis

We make another assumption that the bridge is narrow so that it can be treated as a beam ($b << l$). For a clamped-clamped beam that moves a small distance comparing to its thickness, the ratio of the restoring force and the deflection of the middle point is a constant, the bridge can be mechanically modeled as a linear spring with the spring constant k_b [11, p. 24] (the subscript b is for bending):

$$k_b = 32Ew\left(\frac{t}{l}\right)^3 \frac{1}{8\left(\frac{s}{l}\right)^3 - 20\left(\frac{s}{l}\right)^2 + 14\left(\frac{s}{l}\right) - 1} \tag{3.4}$$

B. 2D analysis

The above equation can be applied well for a narrow bridge. However, in cases where the bridge width is comparable to its length, bending of plate should be studied. The exact solution for deflection of a rectangular clamped-clamped plate with central loading is difficult to obtained due to boundary conditions of the two free sides. To the best of the author knowledge, there are two methods to solve the deflection of a clamped-clamped plate. The first way is using the Fourier method of separation of variables (i.e. approximate the deflection by infinite series of trigonometric and hyper trigonometric functions) [17]. The second one utilizes the symplectic method that is commonly applied in quantum mechanics and relativity, to solve problems in elasticity [18]. However, those works only solve for the case that pressure q is distributed all over the plate. To find the plate deflection in case the loading pressure is only distributed at the center portion of the plate, this thesis proposes an approximate solution. The principle of minimum potential energy is employed to find a polynomial of coordinate variables that can approximate the deflection surface of the bridge. The procedure to search for such polynomial can be done by the following three steps.

- *Step 1:* Expressing the deflection surface as a polynomial, it is helpful to normalize the deflection w to the thickness t and coordinate variables X, Y to the length l of the plate: $\overline{w} = \frac{w}{t}$, $x = \frac{X}{l}$, $y = \frac{Y}{l}$. The nomalized deflection $\overline{w}$ is then expressed as a polynomial of normalized coordinates x, y:

$$\overline{w} = P(x, y) = \sum_{i,j \ even,\ i+j \leq m} a_{(i+1)(j+1)} x^i y^j \tag{3.5}$$

  where i,j are the power of x, y respectively, m is the maximum power of x or y, $a_{(i+1)(j+1)}$ is the coefficient of the polynomial. The power i and j are even because the deflection w is symmetric in the coordinate system assigned to the plate. As an example, when $m = 4$ the polynomial becomes: $P(x, y) = a_{11} + a_{13}y^2 + a_{15}y^4 + a_{31}x^2 + a_{33}x^2y^2 + a_{51}y^4$. Indices of the coefficents start from 1 but not 0 is for compatibility with Matlab software.

- *Step 2:* Find relationship between the coefficients so that the polynomial satisfies 8 boundary conditions at 4 boundaries. The boundary conditions for clamped and free edges can be found in literature of mechanics like [19, p. 83]. To apply for the bridge studied here, these boundary conditions are written in normalized variables as shown in Table 3.2. The plate length and width are normalized to the plate length: $\bar{l} = \frac{l}{l} = 1$, $\bar{b} = \frac{b}{l}$.

TABLE 3.2: Eight boundary conditions for a clamped-clamped plate in bending

Name	**Meaning**	**Expression**
bc1	Deflection at $x = -\frac{1}{2}$ is zero	$\overline{w}(-\frac{1}{2}, y) = 0$
bc2	Slope at $x = -\frac{1}{2}$ is zero	$\overline{w}'(-\frac{1}{2}, y) = 0$
bc3	Deflection at $x = \frac{1}{2}$ is zero	$\overline{w}(\frac{1}{2}, y) = 0$
bc4	Slope at $x = \frac{1}{2}$ is zero	$\overline{w}'(\frac{1}{2}, y) = 0$
bc5	Bending moment at $y = -\frac{\overline{b}}{2}$ is zero	$\left(\frac{\partial^2 \overline{w}}{\partial y^2} + \nu \frac{\partial^2 \overline{w}}{\partial x^2}\right)_{y=-\frac{\overline{b}}{2}} = 0$
bc6	Shear force and twisting moment at $y = -\frac{\overline{b}}{2}$ is zero	$\left[\frac{\partial^3 \overline{w}}{\partial y^3} + (2-\nu)\frac{\partial^3 \overline{w}}{\partial x^2 \partial y}\right]_{y=-\frac{\overline{b}}{2}} = 0$
bc7	Bending moment at $y = \frac{\overline{b}}{2}$ is zero	$\left(\frac{\partial^2 \overline{w}}{\partial y^2} + \nu \frac{\partial^2 \overline{w}}{\partial x^2}\right)_{y=\frac{\overline{b}}{2}} = 0$
bc8	Shear force and twisting moment at $y = \frac{\overline{b}}{2}$ is zero	$\left[\frac{\partial^3 \overline{w}}{\partial y^3} + (2-\nu)\frac{\partial^3 \overline{w}}{\partial x^2 \partial y}\right]_{y=\frac{\overline{b}}{2}} = 0$

Inserting polynomial $P(x, y)$ into all 8 boundary conditions yields $2m$ linear independent equations in $\frac{m^2+6m+8}{8}$ variables (which is equal to the number of coefficients of P). This system of equations has more variables than equations, meaning that it has infinitely many solutions which can be expressed by $\frac{m^2-10m+8}{8}$ independent parameters (i.e. difference between the number of variables and the number of equations). These parameters are the variational variables that should be solved to determine P.

- *Step 3:* Solve for the aforementioned $\frac{m^2-10m+8}{8}$ variational variables by using the principle of miniumum potential energy applied for the plate [19, p. 344]. The total potential energy of the plate expressed in normalized variables is:

$$\Pi = \int_{-\frac{\overline{b}}{2}}^{\frac{\overline{b}}{2}} \int_{-\frac{1}{2}}^{\frac{1}{2}} \frac{Et^5}{24(1-\nu^2)l^2} \left\{ \left(\frac{\partial^2 \overline{w}}{\partial x^2} + \frac{\partial^2 \overline{w}}{\partial y^2} \right)^2 - 2(1-\nu) \left[\frac{\partial^2 \overline{w}}{\partial x^2} + \frac{\partial^2 \overline{w}}{\partial y^2} - \left(\frac{\partial^2 \overline{w}}{\partial x \partial y} \right)^2 \right] - \frac{24\left(1-\nu^2\right) q l^4}{Et^4} \overline{w} \right\} dxdy \tag{3.6}$$

The total potential energy includes elastic potential energy of the plate (the first two terms in the {} bracket) and the potential energy due to the pressure q (the third term in the {} bracket). Let α_1, α_2, α_3, ... be variational variables, the principle of minimum potential energy requires:

$$\frac{\partial \Pi}{\partial \alpha_1} = 0, \ \frac{\partial \Pi}{\partial \alpha_2} = 0, \ \frac{\partial \Pi}{\partial \alpha_3} = 0, \ \ldots \tag{3.7}$$

Solving this system of equations totally defines polynomial P.

The above procedure can be implemented in Matlab using Symbolic Math Toolbox to help simplify calculation work. The detailed code is presented in Appendix A.1.
After polynomial P is found, the spring constant of the bridge can be expressed as the ratio of the force qbW and the deflection of the middle point $w_c = tP(0,0)$:

$$k_b = \frac{qbW}{tP(0,0)} \tag{3.8}$$

To find a converge solution, the Matlab program is run with increased value of polynomial degree, m, until the relative error of $P(0,0)$ between two successive values of m is less than a defined value.

3.1.3 Derivation of spring constant component due to stretching

When the bridge of an RF MEMS switch deflects a distance comparable to its thickness, stretching of the middle surface of the bridge contributes another restoring force in addition to the linear restoring force caused by bending.
A. 1D analysis
The relationship between restoring force due to stretching and deflection of a beam is nonlinear and proved to be [11, p. 27] :

$$F = k_s w_c^3 \tag{3.9}$$

where the stretching spring constant k_s can be calculated by the formula:

$$k_s = \pi^4 \frac{Ebt}{8l^3} \tag{3.10}$$

Taking the ratio of restoring force due to stretching and that due to bending (using Equation 3.10 and Equation 3.4), relative importance of the two effects can be estimated:

$$\frac{F_s}{F_b} = \frac{\pi^4}{256}\left(\frac{w_c}{t}\right)^2\left[8\left(\frac{s}{l}\right)^3 - 20\left(\frac{s}{l}\right)^2 + 14\left(\frac{s}{l}\right) - 1\right] \tag{3.11}$$

For a bridge's with the width of 80 μm and the length of 280 μm, $\frac{F_s}{F_b} = 0.68\left(\frac{w_c}{t}\right)^2$, meaning that if the switch deflects a distance comparable to its thickness, nonlinear effect contributes two fifths to the total restoring force and should not be neglected.

B. 2D analysis

When the bridge's width is comparable to the its length, the nonlinear spring constant of the bridge due to stretching should be studied in two dimensions analysis. In order to do so, the bridge is modeled as a rectangular membrane loaded with a pressure q at the center. The coordinate system assigned to the membrane is shown in Figure 3.4. The displacement u, v, w are approximated by polynomials of variables X and Y. The following procedure uses the principle of minumum potential energy to find approximate polynomials for displacement variables.

- *Step 1:* Expressing the displacement u, v, and deflection w as polynomials of coordinate variables. For the sake of simplicity, u, v, w and coordinate variables X, Y are normalized to the length l of the memebrane: $\overline{u} = \frac{u}{l}$, $\overline{v} = \frac{v}{l}$, $\overline{w} = \frac{w}{l}$, $x = \frac{X}{l}$, $y = \frac{Y}{l}$. The nomalized values $\overline{u}$, $\overline{v}$ and $\overline{w}$ are then expressed as polynomials of normalized coordinates x, y:

$$\overline{u} = P(x,y) = \sum_{i\ odd, j\ even,\ i+j\leq m} a_{(i+1)(j+1)} x^i y^j \tag{3.12}$$

$$\overline{v} = Q(x,y) = \sum_{i\ even, j\ odd,\ i+j\leq m} b_{(i+1)(j+1)} x^i y^j \tag{3.13}$$

$$\overline{w} = R(x,y) = \sum_{i,j\ even,\ i+j\leq m} c_{(i+1)(j+1)} x^i y^j \tag{3.14}$$

where i, j are the powers of x, y respectively, m is the maximum power of x or y, $a_{(i+1)(j+1)}$, $b_{(i+1)(j+1)}$ and $c_{(i+1)(j+1)}$ are the coefficients of the polynomials. The

TABLE 3.3: Six boundary conditions for a clamped-clamped membrane

Name	**Meaning**	**Expression**
bc1	Deflection u at $x = -\frac{1}{2}$ is zero	$\overline{u}(-\frac{1}{2}, y) = 0$
bc2	Deflection u at $x = \frac{1}{2}$ is zero	$\overline{u}(\frac{1}{2}, y) = 0$
bc3	Deflection v at $x = -\frac{1}{2}$ is zero	$\overline{v}(-\frac{1}{2}, y) = 0$
bc4	Deflection v at $x = \frac{1}{2}$ is zero	$\overline{v}(\frac{1}{2}, y) = 0$
bc5	Deflection w at $x = -\frac{1}{2}$ is zero	$\overline{v}(-\frac{1}{2}, y) = 0$
bc6	Deflection w at $x = \frac{1}{2}$ is zero	$\overline{v}(\frac{1}{2}, y) = 0$

power i is even in Q, R and odd in P and the power j is odd in Q and even in P, R due to the symmetry/antisymmetry properties of u, v, w in the coordinate system assigned to the membrane. As an example, when $m = 4$ the polynomial for $\overline{w}$ becomes: $R(x, y) = a_{11} + a_{13}y^2 + a_{15}y^4 + a_{31}x^2 + a_{33}x^2y^2 + a_{51}y^4$. The index of coefficients start from 1 but not 0 is for compatibility with Matlab software.

- *Step 2:* Find the relationship between coefficients so that the polynomials satisfy 6 boundary conditions at 2 fixed boundaries. The boundary conditions for normalized variables are tabulated in Table 3.3, note that the normalized length of the membrane is 1 and the normalized width is $\overline{b} = \frac{b}{l}$.

  Inserting polynomials $P(x, y)$, $Q(x, y)$, $R(x, y)$ into all 6 boundary conditions yields $(2m - 3)$ linear independent equations in $\frac{3m^2+10m+8}{8}$ variables (which is equal to the total number of coefficients of P, Q and R). This system of equations has more variables than equations, meaning that it has infinitely many solutions which can be expressed by $\frac{3m^2-2m}{8}$ independent parameters (i.e. difference between the number of variables and the number of equations). These parameters are the variational variables that should be solved to determine P, Q and R.

- *Step 3:* Solve for the aforementioned $\frac{3m^2-2m}{8}$ variational variables using the principle of miniumum potential energy applied for the membrane [19, p. 419]. The

total potential energy of the membrane expressed in normalized variables is:

$$\Pi = \int_{-\frac{\bar{b}}{2}}^{\frac{\bar{b}}{2}} \int_{-\frac{1}{2}}^{\frac{1}{2}} \frac{Et^3}{2(1-\nu^2)} \left[\bar{\varepsilon}_x^2 + \bar{\varepsilon}_y^2 + 2\nu\bar{\varepsilon}_x\bar{\varepsilon}_y + \frac{1-\nu}{2}\bar{\gamma}_{xy}^2 - \frac{2(1-\nu^2)l^2}{Et^2} q\bar{w} \right] dxdy \tag{3.15}$$

where $\overline{\epsilon_x}$, $\overline{\epsilon_y}$ and $\overline{\gamma_{xy}}$ are the normalized strain values:

$$\bar{\varepsilon}_x = \frac{d\bar{u}}{dx} + \frac{1}{2}\left(\frac{d\bar{w}}{dx}\right)^2 \tag{3.16}$$

$$\bar{\varepsilon}_y = \frac{d\bar{v}}{dy} + \frac{1}{2}\left(\frac{d\bar{w}}{dy}\right)^2 \tag{3.17}$$

$$\bar{\gamma}_{xy} = \frac{d\bar{u}}{dy} + \frac{d\bar{v}}{dx} + \frac{d\bar{w}}{dx}\frac{d\bar{w}}{dy} \tag{3.18}$$

The expression on the right hand side of Equation 3.15 includes stretching potential energy of the plate (the first four terms in the [ ] bracket) and the potential energy due to the pressure q (the fifth term in the [ ] bracket). Let α_1, α_2, α_3, ... be variational variables, the principle of minimum potential energy requires:

$$\frac{\partial\Pi}{\partial\alpha_1} = 0, \ \frac{\partial\Pi}{\partial\alpha_2} = 0, \ \frac{\partial\Pi}{\partial\alpha_3} = 0, \ \ldots \tag{3.19}$$

Solving this system of equations totally defines polynomial P, Q and R.

The above procedure can be implemented in Matlab using Symbolic Math Toolbox to help simplify calculation work. The detailed code is presented in Appendix A.2.
After polynomial R is found, the stretching spring constant of the membrane can be expressed as the ratio of the force qbW and the third order of middle point deflection $w_c = tR(0,0)$:

$$k_s = \frac{qWb}{[tR(0,0)]^3} \tag{3.20}$$

To find a converge solution, the Matlab program is run with increased value of polynomial degree, m, until the relative error of $R(0,0)$ between two successive values of m is less than a defined value.

3.1.4 Derivation of spring constant component due to residual stress

In this section, the bridge of the switch is assumed to have an axial residual stress:

$$\sigma_x = T_0,\ \sigma_y = 0 \tag{3.21}$$

In many cases, the residual stress can be biaxial:

$$\sigma_x = \sigma_y = T_0 \tag{3.22}$$

However, due to the two free boundaries of the bridge, the biaxial stress will soon be relaxed into axial stress:

$$\sigma_x = T_0(1-\nu),\ \sigma_y = 0 \tag{3.23}$$

A. 1D analysis

Residual stress induced in fabrication process can contribute a component to the spring constant and thus stiffen the bridge. The 1D analysis of the stiffness caused by residual stress has been studied in [11, p. 26]. With an axial stress $\sigma_x = T_0$ distributed along the length of the bridge, the stress-induced stiffness of the bridge can be expressed by:

$$k_r = \frac{8T_0bt}{l} \times \frac{1}{3-2(s/l)} \tag{3.24}$$

The restoring for due to residual stress is proportional to the deflection w_c by the constant k_r.

B. 2D analysis

In this part, a procedure to find the stress-induced stiffness of the bridge is presented. The principle of minimum potential energy is employed to find polynomials of variables x and y that can approximate the displacement u and the deflection w of the bridge. The procedure to search for such polynomial can be done by the following three steps.

- *Step 1, Step 2:* Similar to the Step 1 and Step 2 of the Procedure presented in Subsection 3.1.3
- *Step 3:* Solve for the $\frac{3m^2-2m}{8}$ variational variables by using the principle of miniumum potential energy. The total potential energy of the bridge deflected with the presence of residual stress is expressed in normalized variables as:

$$\Pi = \int_{-\frac{\overline{b}}{2}}^{\frac{\overline{b}}{2}} \int_{-\frac{1}{2}}^{\frac{1}{2}} tl^2 T_0 \left[\overline{\varepsilon}_x - \frac{l}{tT_0} q\overline{w} \right] dxdy \tag{3.25}$$

where $\overline{\epsilon_x}$ is normalized strain in x direction:

$$\overline{\varepsilon}_x = \frac{d\overline{u}}{dx} + \frac{1}{2}\left(\frac{d\overline{w}}{dx}\right)^2 \tag{3.26}$$

The expression on the right hand side of Equation 3.25 includes potential energy of the plate due to residual stress (the first term in the [ ] bracket) and the potential energy due to deflection under the pressure q (the second term in the [ ] bracket). Let α_1, α_2, α_3, ... be variational variables, the principle of minimum potential energy requires:

$$\frac{\partial \Pi}{\partial \alpha_1} = 0, \ \frac{\partial \Pi}{\partial \alpha_2} = 0, \ \frac{\partial \Pi}{\partial \alpha_3} = 0, \ \ldots \tag{3.27}$$

Solving this system of equations totally defines polynomial P and R.

The above procedure can be implemented in Matlab using Symbolic Math Toolbox to help simplify calculation work. The detailed code is presented in Appendix A.3.
After polynomial R is found, the spring constant due to residual stress can be expressed as the ratio of the force qbW and the middle point deflection $w_c = tR(0,0)$:

$$k_r = \frac{qWb}{tR(0,0)} \tag{3.28}$$

To find a converge solution, the Matlab program is run with increased value of polynomial degree, m, until the relative error of $R(0,0)$ between two successive values of m is less than a defined value.

3.1.5 Effects of etching holes

Beside promoting etching and releasing, etching holes bring another benefit that it can lower the air damping under the bridge and hence, decrease the switching time. Following are parameters that can be altered due to etching holes:

- *Effective Young's modulus*, *Poisson's ratio* and *residual stress* of the bridge reduce as the total hole area increases. According to [20], for holes distributed in square

perforation pattern with $d_{hole}/pitch = 0.625$, the effective Young's modulus, Poisson's ratio and the effective residual stress are:

$$E_{eff} = 0.76E, \quad \nu_{eff} = 0.85\nu, \quad T_{0eff} = 0.68T_0 \tag{3.29}$$

- *Down-state capacitance* is reduced; however, up-state capacitance is unchanged given that the hole diameter is less than three times the air gap, thanks to fringing field effect [11, p. 29].
- *The damping constant* is lowered as the area of the bridge is reduced. Furthermore, since air can escape not only at the bridge boundaries but also at perimeter of holes, the spring force due to compression of gas is significantly reduced.

3.1.6 Electromechanical analysis of RF MEMS switch

A. Static study

To make calculation of electrostatic force easy, the delection is assumed to be uniform over the central portion of the bridge and is equal to the deflection of the central point. This assumption is reasonable since the air gap is small comparing to the length and the width of the bridge and the bridge moves only one third of the air gap prior to pull-in. Knowing the spring constant of the bridge, the deflection of the central point, w_c, can be found the by the equation of balanced forces:

$$\frac{\varepsilon_0 bWV^2}{2\left(g_0 + \frac{t_d}{\varepsilon_r} + w\right)^2} \times f_{fringing} + (k_b + k_r)w + k_s w^3 = 0 \tag{3.30}$$

In equation 3.30, the factor $f_{fringing}$ accounts for the effect of fringing field and is defined as the ratio of the total electrostatic force and the parallel-plate electrostatic force: F_e/F_{pp}. It should be noted that the deflection w is negative if we choose to use the upward z axis as shown in Figure 3.1. When stretching effect is neglected, the pull-in voltage can be expressed as a closed-form expression:

$$V_{pull-in} = \sqrt{\frac{8(k_b + k_r)}{27\varepsilon_0 Wb} \times \left(g_0 + \frac{t_d}{\varepsilon_r}\right)^3 \times \frac{1}{f_{fringing}}} \tag{3.31}$$

If stretching effect is considerable, a Matlab program can be written to solve Equation 3.30.

B. Dynamic study

It is desirable to make the MEMS switch response as fast as possible to the DC control

voltage and thus, switching time is an important factor when designing RF MEMS switch. The shorter the switching time, the better can the switch response to control signal. The switching time can be improved by either increasing the stiffness of the bridge or lowering the damping effect.
The time-dependent equation for an RF MEMS switch in 1D analysis is:

$$F_e + m\frac{d^2w}{dt^2} + b\frac{dw}{dt} + (k_b + k_r)w + k_s w^3 = 0 \tag{3.32}$$

where $m,\ b,\ k_b,\ k_r,\ k_s$ are the lumped mass, damping coefficient and spring constant component due to bending, stretching and residual stress respectively, F_e is the electrostatic force. When the switch is actuated in vacuum, the damping force can be neglected. In case the deflection is small and residual stress can be neglected, the swiching time can be calculated as a function of actuation voltage and angular resonance frequency of the bridge [11, p. 68]:

$$t_s = 3.67\frac{V_p}{V_{act}\omega_0} \tag{3.33}$$

where $V_p,\ V_{act}$ are the pull-in voltage and actuation voltage respectively, ω_0 is the angular resonace frequency of the bridge. The angular resonance frequency can be calculated using the Rayleigh-Ritz method. For example, for a doubly-clamped beam in pure bending, with the trial function $w = \frac{c}{2}\left[1 + cos(\frac{2\pi x}{l})\right]$, angular resonance frequency is found to be:

$$\omega_0 = \frac{2}{3}\pi^2\frac{H}{l^2}\sqrt{\frac{E}{\rho_m}} \tag{3.34}$$

In the above equation,$H,\ l$ are the thickness and length of the bridge, ρ_m is the density of the bridge material. If stretching and residual stress is considerable, the terms including $k_r,\ k_s$ in Equation 3.32 should be taken into account.
When the bridge is actuated in air, squeezed-film damping due to the air gap is also considered. The pressure of air under the bridge can be describe by the Reynold's equation [21, p. 102]:

$$\frac{\partial}{\partial x}\left(\rho\frac{h^3}{\mu}\frac{\partial P}{\partial x}\right) + \frac{\partial}{\partial y}\left(\rho\frac{h^3}{\mu}\frac{\partial P}{\partial y}\right) = 12\frac{d\,(h\rho)}{dt} \tag{3.35}$$

or the alternative form which is used by COMSOL software:

$$-\nabla\,(\rho h\mathbf{u}) = \frac{d\,(h\rho)}{dt} \tag{3.36}$$

For the Equation 3.35 or 3.36 to be valid, it is required that the Modified Reynold's Number is less than unity: $R_s = \frac{\omega h^2 \rho}{\mu} << 1$, which is usually hold for RF MEMS switch. For example, for a gold bridge having length of 280 μm, width of 80 μm and thickness of 2 μm, the air gap of 2 μm, air viscosity of $18.45 \times 10^{-6} Pa.s$ and angular frequency of 0.3 MHz (which is equal the angular resonace frequency of the bridge), the value of R_s is 0.07, well below unity. Solution of Reynold's equation can be found in MEMS textbook like [21] or [22].

3.1.7 Electromechanical simulation of RF MEMS switch

A. Building the switch geometry

The computer models for MEMS shunt switches are built with the same parts and layers as the real, fabricated switches by PhD Deokki Min[10, p. 47]. All dimensions are made parametric, making it easier to investigate the effects of each dimension. Thanks to symmetry, one quarter of a switch is modeled, saving computation resources and time but still giving accurate results. The geometry of a switch is shown if Figure 3.5. Figure 3.6 illustrates another switch which has perforated bridge, hole diameter is 3.75 μm and distance between two holes is 6.25 μm.

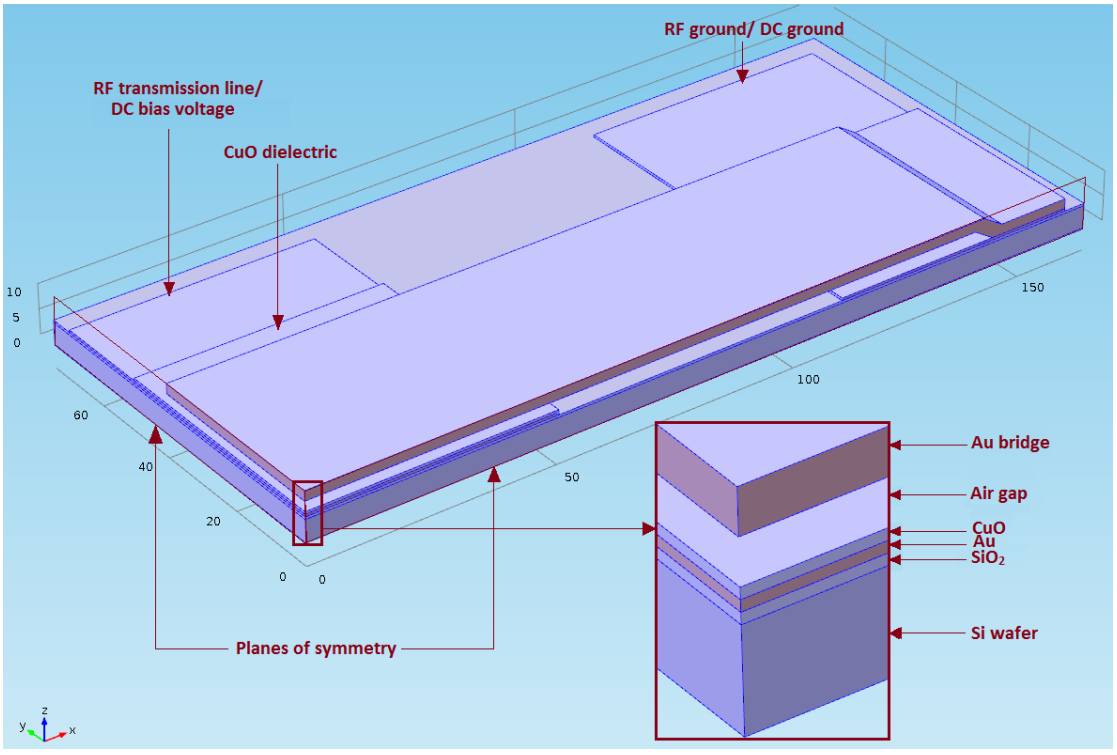

FIGURE 3.5: One quarter of a switch built in COMSOL

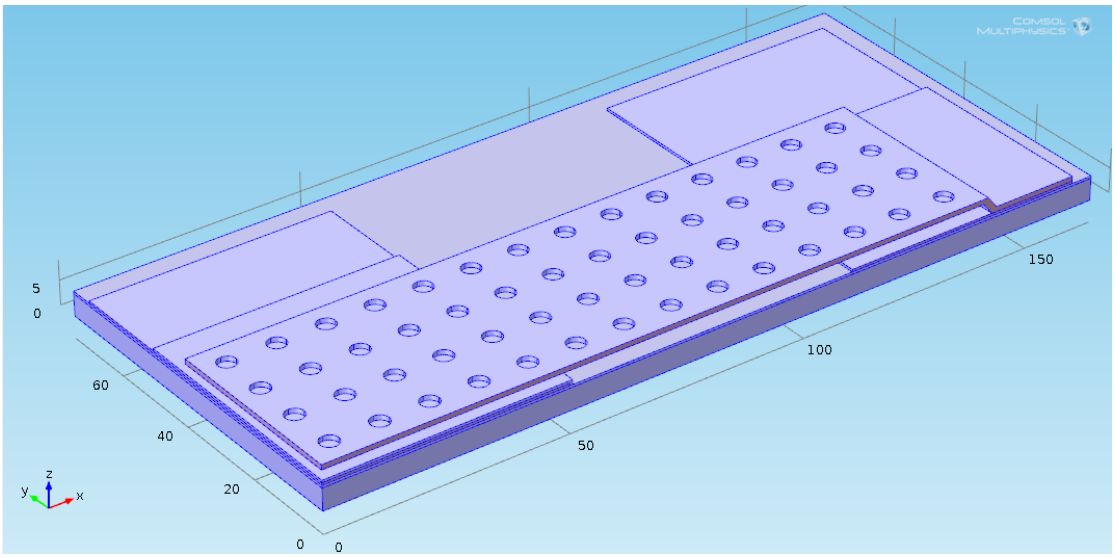

FIGURE 3.6: A switch with perforated bridge

B. Meshing

A user-controlled mesh is used, element size at critical parts (the bridge, the bottom electrode and the dielectric layer) are set smaller than at other parts. The element size is an important factor, since a finer mesh would give more accurate results but with the cost of increased simulation time. To find an efficient meshing scheme, the simulation is first run with a relative coarse mesh. The mesh is then made finer, the simulation is run again and the relative error between results of the two simulation works is then calculated. The above procedure is repeated until a relative error of less than 1 percent is obtained. The final mesh is show in Figure 3.7, with finer quality in blue regions.

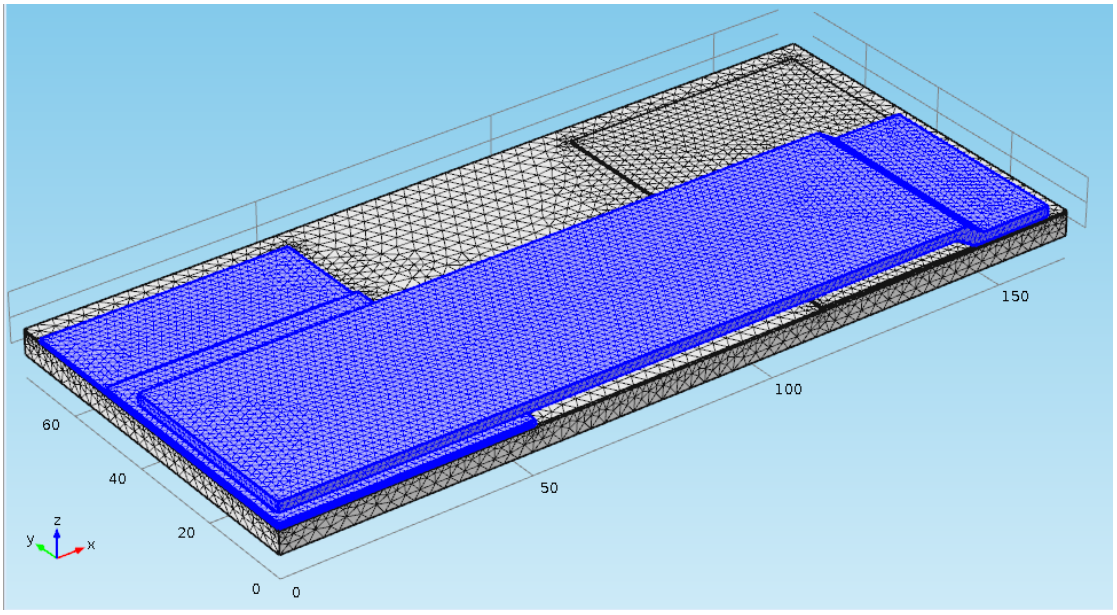

FIGURE 3.7: Final mesh, with finer quality highlighted in blue regions

C. Stationary study

First, stationary step is used to simulate the deflection of the switch and find the pull in voltage. The physics *Electromechanics* is chosen because it couples *Electrostatics interface*, *Structural mechanics interface* and *Moving mesh feature*, which are suitable for simulating electrostatically actuated device. To model an RF MEMS switch, the following configurations are made:

- *Linear elastic material*: domains of the gold bridge, transmission line, RF/DC ground plane and silicon wafer are selected. In these domains, only equations for structure mechanics are included. Electrostatic force acting on their surfaces are applied in the *Electromechanical interface* default node. The residual stress can be included by creating a sub-node named *Initial stress and strain*.
- *Fixed mesh*: the fixed geometry are assigned fixed mesh.
- *Fixed constraint*: the fixed geometry are assigned zero displacement vector.
- *Symmetry*: specifying symmetric boundaries for structural mechanics. The displacement normal to these boundaries are zero.
- *Ground*: outer surfaces of the bridge and the RF/DC ground planes are selected.
- *Terminal*: outer surfaces of the bottom electrode are selected and assigned the value of actuation voltage. The actuation voltage is swept over a range of values to find corresponding deflection and pull-in voltage.
- *Prescribed mesh displacement*: due to symmetry, mesh boundaries on the two planes of symmetry are restricted not to move in perpendicular direction.

The voltage between the bridge and the bottom electrode is swept to investigate the deflection under different values of biased voltage. The pull-in voltage is found when the solver fails to find a converge solution. That is because when pull-in phenomenon happens, the bridge goes a distance larger than the air gap which then causes air mesh elements at the middle of the bridge inverted.

For after pull-in simulation, a *Solic Mechanics* study is perfomed. A *Contact Pair* node is added to specify mechanical contact between the top surface of the dielectric layer and the bottom surface of the bridge. The software can simulate the situation when the two surfaces approach and come to contact with each other. A mechanical pressure is specified at the bottom surface of the bridge, as a replacement for electrostatic force. To help the solver converge, the mechanical pressure is swept from a value which is enough for the bridge and the dielectric layer come in contact to the electrostatic pressure when the bridge totally lies on the dielectric layer.

D. Dynamic study

In this part, the switching time is studied by using the transient solver of COMSOL Multiphysics. The *Thin-film damping* node is added to the model to study the squeezed-film damping in the air gap. In the *Fluid film properties* sub-node, the viscosity of air is set to 18.45×10^{-6} $Pa.s$ [21, p. 92], the air film thickness is set equal to the air gap and ambient pressure is the atmospheric pressure. The air gap at the central region is meshed finer to improve precision of the solution when the bridge comes very close to the dielectric layer. The time step is 0.5 ms.

The switching time is simulated for both cases: in air and in vacuum, in order to see the effect of air damping. Switches with holes on bridge are also investigated.

3.2 Electromagnetic analysis and simulation of capacitive RF MEMS shunt switch

As its name suggests, the switch is connected in shunt configuration between the transmission line and two ground planes, as can be seen in Figure 2.2 and 2.3. Depending on the actuation voltage, the switch may be in up-state where the transmission line is undisturbed or in down-state where the transmission line in grounded. There are two concepts usually used to evaluate RF performance of an RF MEMS switch: (up-state) insertion loss and (down-state) isolation. The insertion loss is a parameter that quantify how much of the RF energy is lost due to the insertion of the switch above the transmission line. In up-state, the insertion loss has a negative, small (in magnitude) value (-0.04 to -0.1 dB for a well-designed switch [11]). The isolation is used to quantify how effective the switch can stop the power going to output port. It is defined as the dB value of square of magnitude of S_{21}. In down-state, since the output power is very small comparing to the input power, the isolation holds a negative, large (in magnitude) value (at least -20 dB at 10-50 GHz for a well-designed switch [11]). This section studies on effects of geometry on insertion loss and isolation of the switch, so as to find a design that can satisfy the aforementioned conditions.

3.2.1 Electromagnetic analysis of capacitive RF MEMS shunt switch

In RF domain, the switch is modeled as an RLC circuit with inductance L, resistance R and variable capacitance C. The ratio of down-state capacitance to up-state capacitance is called capacitance ratio of the switch. The theory in Section 2.3 can be used to calculate S-parameters of an RF MEMS switch. The RF model of a switch is shown in Figure 3.8, where the switch is decomposed into R_s, L_s and C components. Assuming

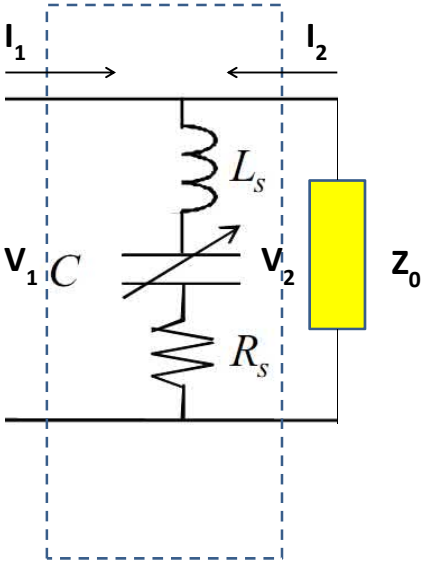

FIGURE 3.8: RF model of an RF MEMS shunt switch

that the terminated load has the same impedance as the transmission line, Z_0, the parameters S_{11} and S_{21} can be calculated as following:

$$S_{11} = \frac{b_1}{a_1} \; when \; a_2 = 0$$

$$S_{11} = \frac{V_1 - I_1 Z_0}{V_1 + I_1 Z_0} = \frac{Z_s \parallel Z_0 - Z_0}{Z_s \parallel Z_0 + Z_0} = \frac{-Z_0}{2Z_s + Z_0} \tag{3.37}$$

$$S_{21} = \frac{b_2}{a_1} \; when \; a_2 = 0$$

$$S_{21} = \frac{V_2 - I_2 Z_0}{V_1 + I_1 Z_0} = \frac{V_1 - I_2 Z_0}{V_1 + I_1 Z_0} = \frac{2Z_s}{2Z_s + Z_0} \tag{3.38}$$

Here, Z_s is the total impedance of the switch, including R_s, L_s and C components. Due to symmetry, it is apparent that $S_{22} = S_{11}$ and $S_{12} = S_{21}$.
The insertion loss (IL) and isolation (IS) can be calculated using the S_{11} and S_{21} parameters mentioned above [11]:

$$IL = 1 - |S_{11}|^2 - |S_{21}|^2 \tag{3.39}$$

or

$$IL(dB) = 10log(|S_{11}|^2 + |S_{21}|^2) \tag{3.40}$$

$$IS(dB) = S_{21}(dB) = 10log|S_{21}|^2 \tag{3.41}$$

3.2.2 Electromagnetic simulation of capacitive RF MEMS shunt switch

The electromagnetic simulation in this subsection uses the *Electromagnetic Waves, Frequency Domain Interface* in *RF Module* of COMSOL. The whole switch geometry is studied instead of only one quarter as before since input and output RF signal should now be applied and measured at the two ends of the coplanar wage guide. All dimensions and settings are kept the same as for electromechanical simulation, except for the following modifications:

- The gap between transmission line and RF ground plane is adjusted so that the characteristic impedance of the coplanar wave guide is equal to 50 Ω. For a wafer thickness of 525 μm, an SiO_2 layer of 500 nm and bottom electrode width of 100 μm, the required gap is 52.5 μm [23, p. 176] [24].

- The actual thickness of high-ρ silicon wafer is 525 μm, which is very large comparing with the thickness of the dielectric layer (300 nm), resulting a very large number of mesh elements and degrees of freedom. Since the important information for RF simulation is the effective dielectric constant of the coplanar wage guide, the computational burden can be avoided by simulating with a small wafer thickness and change the dielectric constant of the wafer so that the resulting effective dielectric constant of the CPW is the same as before.

- It should be noted that CuO is a semiconductor material. To account for this, the *Electrical Conductivity* of CuO material is set to a value taken from literature [25].

Also in down-state of the switch, we assume that the bottom surface of the bridge and the top surface of the dielectric layer are in total contact.

A. Boundary conditions

The detailed boundary conditions are as follows and also illustrated in Figure 3.9:

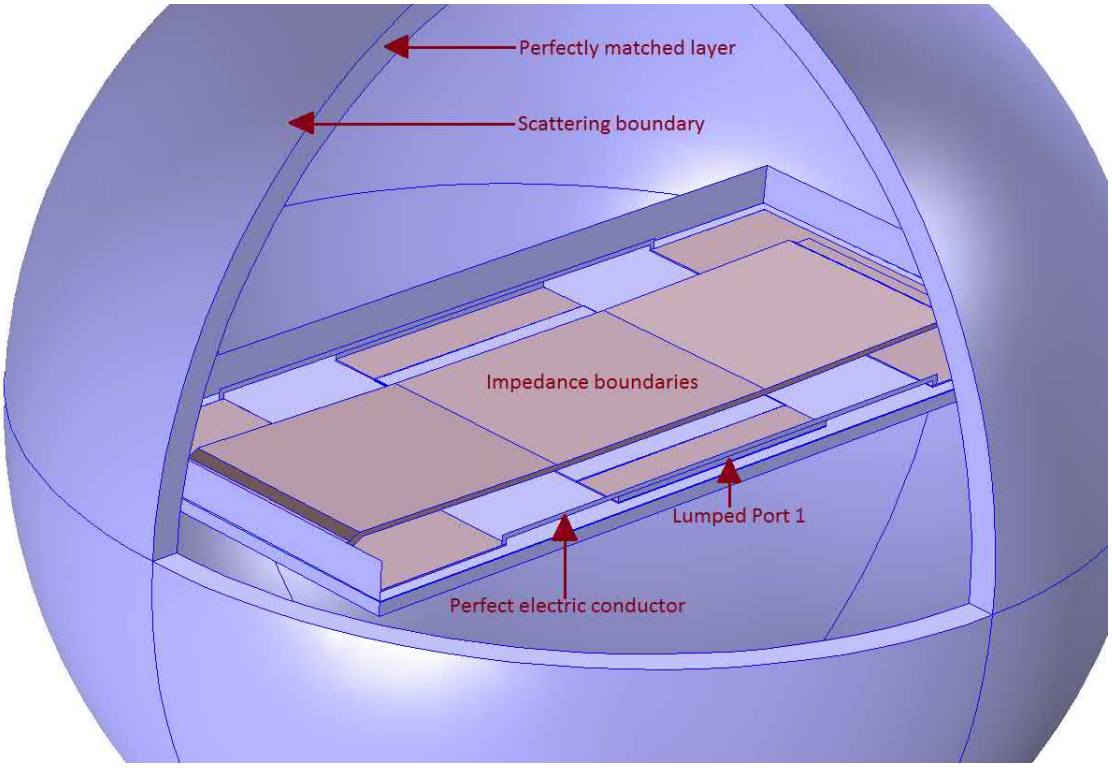

FIGURE 3.9: Boundary conditions for RF simulation

- *Lumped Port 1* and *Lumped Port 2* are specified at the two ends of transmission line. Both have the characteristic impedance of 50 Ω. At the lumped port 1, an excitation voltage of 1 V is applied.
- *Perfect Electric Conductor* is assigned to small conductor lines connecting the two RF ground planes for each lumped port.
- *Scattering Boundary Condition* is applied on a spherical surface encapsulating outside the switch. This surface is transparent for RF scattered wave coming from the switch and help avoid reflection of the scattered wave. Also, to further help absorb the outgoing wave, a thin spherical *Perfectly Matched Layer* is added right within the scattering boundary.
- *Impedance Boundary Condition* is assigned to the gold surface to account for the conductor loss. The relative permittivity, relative permeability and electrical conductivity are taken from gold material.

B. Mesh

In electromagnetic simulation, a rule of thumb is that the maximum element size should

be less than one fifth of the wave length to ensure precision. In this thesis, the frequency range is under 100 GHz, meaning that the maximum mesh size should be less than 600 μm. This condition easily holds since dimensions of the switch are much smaller than this value.

3.3 Deposition and characterization of Copper(II) oxide

3.3.1 An investigation on high-κ metal oxides

As has been referred to in Chapter 1, it is desirable to use a high dielectric constant material for capacitive RF MEMS switch, so as to obtain a high down-state capacitance and as a result, improve the capacitance ratio and down-state isolation of the switch. In this thesis, an investigation on metal oxides is carried out to search for a replacement for traditional dielectric materials in RF MEMS switch - silicon oxide and silicon nitride. The intended deposition method is first evaporating metal thin film, then thermally oxidizing the deposited metal film into oxide film. The advantages of thermal evaporation is that it is an easy method for depositing a wide range of metals. Furthermore, deposited films have smooth surface and since evaporation is carried out in vacuum, the films are relatively pure. The investigation is carried out as follows. The other two physical vapor deposition methods, e-beam evaporation and sputtering, are also considered, as they can be alternative methods when thermal evaporation is not possible.

- Listing all metals that can be evaporated by thermal evaporation, e-beam evaporation or sputtering. At this step, we refer to the guide from Vacuum Engineering & Materials Company [26].
- Eliminating from the list metals that are toxic such as Lead or Beryllium or radioactive like Uranium. Also, metals having oxides that decomposes, loses oxygen or have high conductivity are removed.
- Finding in literature dielectric constants of oxides of the remaining metals. At this step, we refer to a compilation on dielectric constants of various materials [27]. Oxides that have dielectric constant of less than 10 are eliminated from the list. In the scope of a master thesis, metals that are rare or oxides that have dielectric constant unpublished in literature are not considered. The remaining metals are shown in Table 3.4, together with the deposition method and their corresponding oxides. Some values of dielectric strength are also shown, together with the reference source [27] [28].

TABLE 3.4: Metals which have high-κ oxides and their deposition method

Metal	Evaporation			Sputter	Oxide		
	Thermal	E-beam	Remark		Formula	κ	$E_{break\text{-}down}$ (MV/cm)
W		✓	Film hard and adherent	✓	WO_3 (ε_{11})	90000 [27]	
W		✓	Film hard and adherent	✓	WO_3 (ε_{33})	60000 [27]	
W		✓	Film hard and adherent	✓	WO_3 (ε_{22})	40000 [27]	
Mn		✓			MnO_2	10000 [27]	
					MnO	12.8, 18 [27]	
Ti		✓	Alloys with refractory metals	✓	TiO_2 (ε_{33})	170 [27]	1 - 3.2 [28]
					TiO_2 ($\varepsilon_{11}, \varepsilon_{22}$)	86 [27]	
					TiO_2	60, 95 [28]	
Zr		✓			ZrO_2	12.5 [27], 29 [28]	3.8 [28]
Ta		✓	Good film	✓	Ta_2O_5	19 - 28 [28]	2.5 - 6 [28]
Ce		✓	Film oxidizes easily		CeO_2	7, 28 [27]	
Fe		✓	Film hard, smooth		Fe_3O_4	20 [27]	
Hf		✓			HfO_2	20 [28]	3 - 4.7 [28]
Cu	✓	✓	Adhesion is not good		CuO	18.1 [27]	
Sn	✓	✓			SnO_2	9, 14 [27]	
Cr	✓	✓	Adherent film, high rate possible		Cr_2O_3	13.3 [27]	
Co		✓	Alloy with refractory metal		CoO	12.9 [27]	
Fe		✓	Film hard, smooth		Fe_2O_3	12 [27]	
Ni	✓	✓	Smooth, adherent film, forms alloy with refractory metal	✓	NiO	9.7, 11.9 [27]	
Al	✓	✓		✓	Al_2O_3	9.34, 11.54 [27]	6.2, 7.2 [28]
						8.5 [28]	

- In Table 3.4, there are ten oxides having dielectric constant larger than 15. Among them, CuO can be thermally evaporated and is chosen to study in this thesis.

In the next two parts, the method for deposition and measurement of CuO is presented.

3.3.2 Deposition of Copper (II) Oxide

The thermal oxidation of thermally evaporated copper film has been described in previous work [29] [25] [10]. In work by Papadimitropoulos et al. [29] and Valladares et al. [25], the pristine copper film before oxidation is 50 nm and 100 nm, respectively. In work by Deokki [10], 250 nm copper was deposited but only approximately 75 nm of CuO is reported, meaning the copper film is not totally oxidized.

For RF MEMS switch, it is attractive to make the dielectric layer as thin as possible, so as to archive high capacitance ratio and high isolation. However, the fact that RF MEMS capacitive switches normally use a relatively high DC actuation voltage may hinder this possibility due to the high field strength. For example, a typical actuation voltage of 30 V could create across a 100 nm thick dielectric layer an electrical field of 3 MV/cm, which is a limit for many dielectric materials as can be seen in Table 3.4. As can be seen from Deokki simulation work [10, p. 52], among the range of thickness from 50 nm to 300 nm, 300 nm thickness would give the best isolation for his switch design

in our targeted K_a band (more than 30 dB). In this thesis, the targeted CuO oxide layer for deposition and characterization is 300 nm for that reason. In this subsection, three aspects are under investigation. Firstly, we want to find a combination of temperature and time that would give a smooth, homogeneous oxide surface. Secondly, in most cases, the metal film thickness increases during oxidation due to the insertion of oxygen atoms. Since an exact thickness of dielectric film is desirable for fabrication of MEMS switch, it is necessary to find the ratio of copper oxide thickness to pristine copper thickness. Finally, the effect of oxygen flow on oxidation of copper is studied to decide whether oxygen flow is needed to improve the oxidation process. The detailed instruments and method are described in the following paragraphs.

A. Instruments

- *Thermal Evaporator Moorfield MiniLab T25M* is used for thermal evaporation. The machine has four discrete crucibles filaments for resistive evaporator, can load a whole 4-inches wafer and has quartz sensor for measuring thickness. The highest vacuum level is 10^{-6} $mBar$ and the distance from source to wafer is 18 cm.
- *Tube Furnace GSL-1100* helps thermally oxidize the metal film. The furnace has a 2-inches diameter quartz tube with operating temperature up to 1100 °C. Gas supply can also be installed.
- *Optical Microscope Leica DM4000M* and *DEKTAK Profilometer* are used for observation and thickness measurement.

B. Experimental details

Since the expansion of copper film through oxidation is unknown, a trial thickness of 300 nm copper is chosen. The expansion ratio can then be deduced from the final oxide thickness and the pristine copper thickness. First, 15 nm chromium is evaporated on SiO_2/Si subtrate as an adhesion layer. Copper is then evaporated on top of the chromium layer, the chamber pressure is $5 \times 10^{-6} mBar$ and evaporation rate is 1.3 $\AA/s$. The thickness of copper film is 300 nm as reported by the quartz sensor. The copper film is etched using a mask with small opening lines to help measure the thickness of metal film or oxide film later. The wafer is then cut into small pieces, which would be put into the furnace for annealing. The temperature of the furnace is slowly raised until it reaches a certain value. In this experimental work, that value is from 350 °C to 500 °C since copper can be totally converted to copper (II) oxide at above 350 °C [29] [25]. The samples are kept at the constant temperature for a defined annealing time. This annealing time is important for the film to be converted totally in to oxide.

The probing annealing time are 30 minutes, 60 minutes or 120 minutes. The oxygen gas can be optionally supplied into the quartz tube. The samples are then cooled down naturally to room temperature. The thickness of metal film before and after oxidation is measured by stylus profilometer and the surface of oxide film is observed and captured by optical microscope.

After the expansion ratio is calculated from the 300 nm copper samples, another sample with only 125 nm copper is prepared in an attempt to obtain exactly 300 nm oxide. This time, the copper film is deposited on top of SiO_2 layer and is carefully scratched instead of etched. The annealing temperature is 350 °C and the time is 120 minutes. It is also re-annealed in 60 minutes to confirm the result of 120 minutes annealing time.

3.3.3 Measurement of dielectric constant of Copper (II) Oxide

A. Theory

The dielectric constant of a dielectric material can be calculated by measuring transmission coefficient (S_{21}) of a coplanar wave guide deposited on top of a thin layer of that dielectric (Figure 3.10). First, the effective dielectric constant of the CPW is extracted

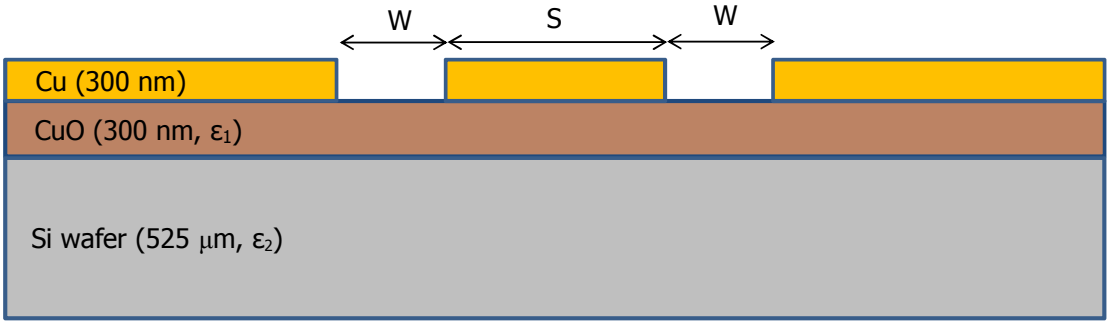

FIGURE 3.10: CPW structure used to measure dielectric constant of CuO

from the phase of S_{21} [10]:

$$\varepsilon_{eff} = \left(\frac{\Phi_{S_{21}}}{360} \times \frac{c}{fl} \right)^2 \tag{3.42}$$

In the above equation, ε_{eff} is the effective dielectric constant of the CPW, $\Phi_{S_{21}}$ is the phase of S_{21} in degree, f is the frequency, l is the CPW transmission line length and c is the speed of light. The dielectric constant of dielectric material is then calculated by conformal mapping [24]:

$$\varepsilon_2 = \varepsilon_1 + \frac{\varepsilon_{eff} - [1 + q_1(\varepsilon_1 - 1)]}{q_2} \tag{3.43}$$

Here, ε_1 and ε_2 are the dielectric constants of wafer and dielectric material, respectively, q_1 and q_2 are geometrical factors dependent on the CPW transmission line width, CPW gap, thickness of wafer and thickness of oxide film. For detailed calculation, readers can refer to mathematical analysis by Carlsson [24]. In case conductor loss is significant, a two measurement method is used: first, measure effective dielectric constant of a CPW with both dielectric layer and wafer (ϵ_{eff}), then measure that value of an identical CPW deposited directly on wafer ($\epsilon_{eff}^{'}$) [30]. The equation for calculating ϵ_2 is now independent on conductor loss:

$$\varepsilon_2 = \varepsilon_1 + \frac{1 + q_1(\varepsilon_1 - 1)}{q_2} \frac{\varepsilon_{eff} - \varepsilon_{eff}^{'}}{\varepsilon_{eff}^{'}} \tag{3.44}$$

B. Experimental

The process flow to make CPW structures is illustrated in Figure 3.11 and described

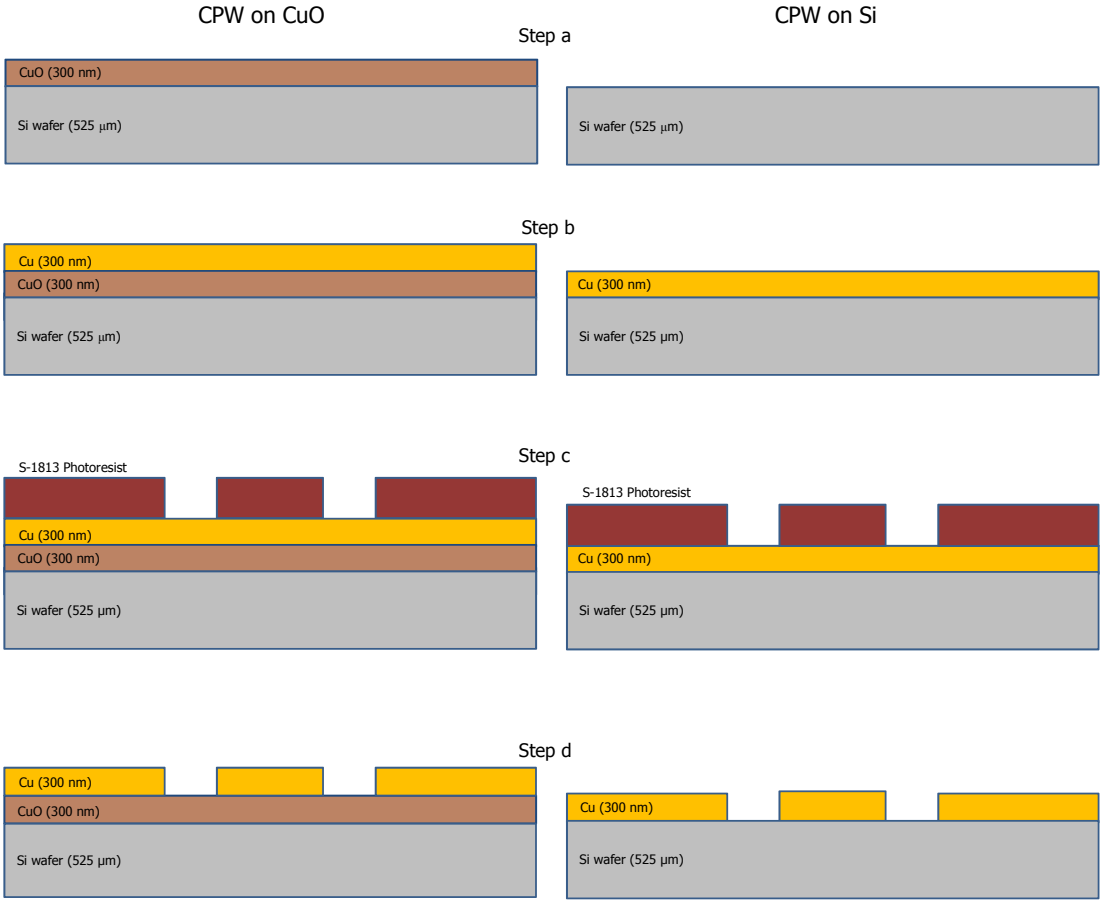

FIGURE 3.11: Fabrication process to make CPW structures

as follows. In order to perform a two measurement method (Equation 3.44), a high-ρ Si wafer is cut into halves. One half is cover with 125 nm evaporated Cu, then it is annealed at 350 °C in air for 120 minutes to form CuO (step a). The both halves are

then evaporated with 300 nm Cu (step b) and then etched to form CPW structures. The etching process is as follows. First, a lithography process is performed with conventional S-1813 positive photoresist. A CPW mask from Deokki's project is reused. After the photoresist layer is developed (step c), Cu is etched using a base solution. The original solution is diluted by water: 60 ml of water is added into 10 ml of old etchant to form 70 ml of new, diluted etchant. It is important that the etchant would not etch away the CuO layer beneath. To make sure this, two test sample are prepared: one with 150 nm Cu, the other with 188 nm CuO. The two are put into the diluted etchant solution for 50 seconds, the time that is just enough for all Cu layer disappear. While the Cu layer is etched with the speed of 3 nm/s, the remained CuO layer is 185 nm thick, meaning it is almost left intact. The etching is then performed on the Cu layer on two wafer halves. The Cu layer is observed during etching and the etching process is stop immediately after all Cu layer disappears to prevent etching of CuO layer underneath. Finally, the photoresist layers are stripped (step d).
The CPWs are then measured at Kongsberg Norspace with help from PhD Deokki Min. One parameter important for measuring effective dielectric constant of CPW is its length l (Equation 3.42). The CPW length l is measured by using the optical microscope $LeicaDM4000M$. First, the microscope is calibrated with a standard sample having known length. The CPWs are then captured using $200x$ magnification; since their lengths are in several millimeters range, capturing a whole CPW would requires several tens of images. These images are then combined manually into a large image of the whole CPW. Basing on the $pixel/meter$ ratio obtained from the optical microscope, the exact length of CPW can be found.

3.3.4 Measurement of dielectric strength of Copper (II) Oxide thin film

The dielectric strength, which is the maximum electric field strength that it can withstand without breaking down, is an important parameter for dielectric material used in capacitive MEMS switches. A high-k dielectric material would be useless unless its dielectric strength is large enough to resist the actuation voltage. To the best of the author knowledge, the dielectric strength of thermally oxidized CuO has not yet been reported in literature. This value is investigated in this thesis to evaluate the possibility of utilizing CuO as dielectric material for high isolation RF MEMS switch.
To measure the dielectric strength of CuO, metal-oxide-metal capacitors are made. Figure 3.12 illustrates cross section of a MIM capacitor and how electrical source meter is connected.
The detailed fabrication process of MIM capacitor is as follows. A stack of Cr/Cu/Cr

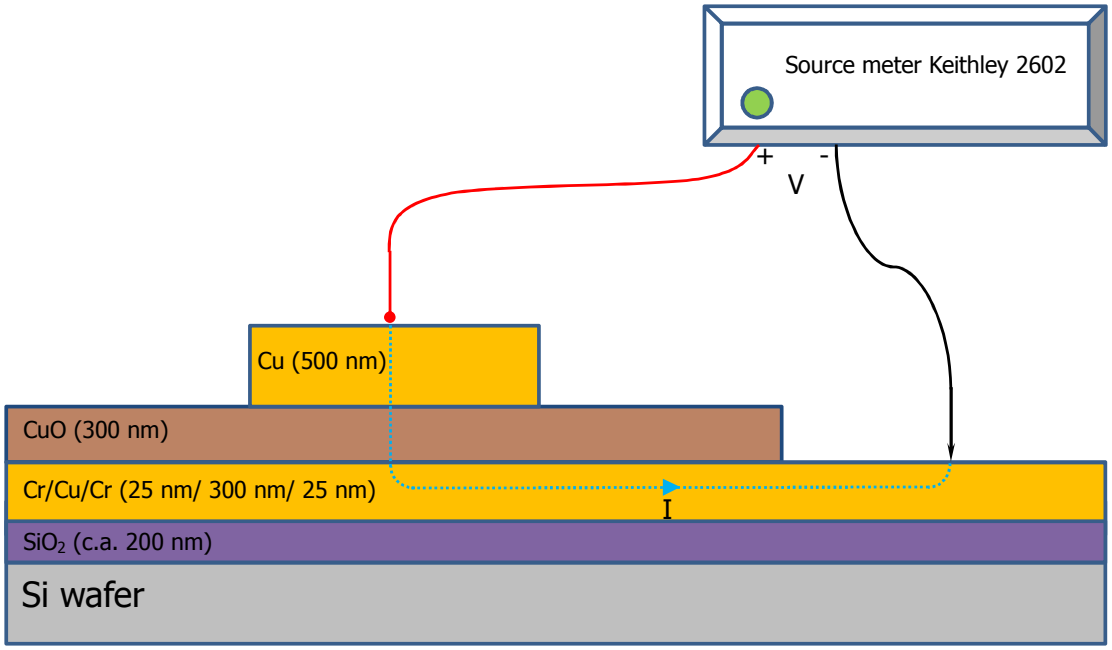

FIGURE 3.12: MIM structure and electrical setting for measuring dielectric strength of CuO

(25 nm/300 nm/35 nm) is evaporated on a SiO_2/Si silicon substrate as the bottom pad for MIM capacitor. The purpose of SiO_2 is to minimize leakage current into Si wafer. The bottom Cr layer is for adhesion promotion and the top Cr layer is for both adhesion and diffusion barrier. A layer of 125 nm copper is evaporated on top of the bottom pad and is then thermally oxidized at 350 °C in air for 120 minutes to form CuO. The thickness of oxide film is confirm by the profilometer to be 300 nm. The substrate is then covered with a shadow mask, a thin aluminium sheet with small drilled holes, and put into evaporator to pattern small, circle top pads for MIM capacitors. The thickness of top pads is 500 nm. The diffusion of oxygen in CuO into the Cu top pad is not considerable since there is very low substrate heating in thermal evaporation [31, p. 138] and the MIM capacitors are measured after fabrication. The measurement is performed using *Keithley 2602 SourceMeter* as illustrated in Figure 3.12. A voltage is applied between the top and bottom pad of MIM capacitor through two needles loaded on a probe station. The needle tip on the top pad is made flat so as it would not penetrate into the top pad and oxide layer. The voltage is swept from zero with the resolution of 0.1 V, the measured current is read 15 seconds after applying a voltage value.

Chapter 4

Results

4.1 Electromechanical analysis and simulation of RF MEMS switch

4.1.1 Fringing field effect

As can be seen in Equation 3.2, the total capacitance is always large than the parallel-plate capacitance due to the added fringing capacitance, which is dependent on the bridge thickness and the air gap. Figure 4.1 shows the relative value C/C_{pp} as a function of bridge thickness and Figure 4.2 shows the relative value C/C_{pp} as a function of air gap. On both figures, the simulation and analysis results are presented; when changing the air gap, the bridge thickness is kept at 1 μm and when changing the bridge thickness, the air gap is kept at 1 μm.
The relative force F/F_{pp} is shown in Figure 4.3 as a function of bridge thickness and in Figure 4.4 as a function of air gap. On both figures, the simulation and analysis results are presented; when changing the air gap, the bridge thickness is kept at 1 μm and when changing the bridge thickness, the air gap is kept at 1 μm.

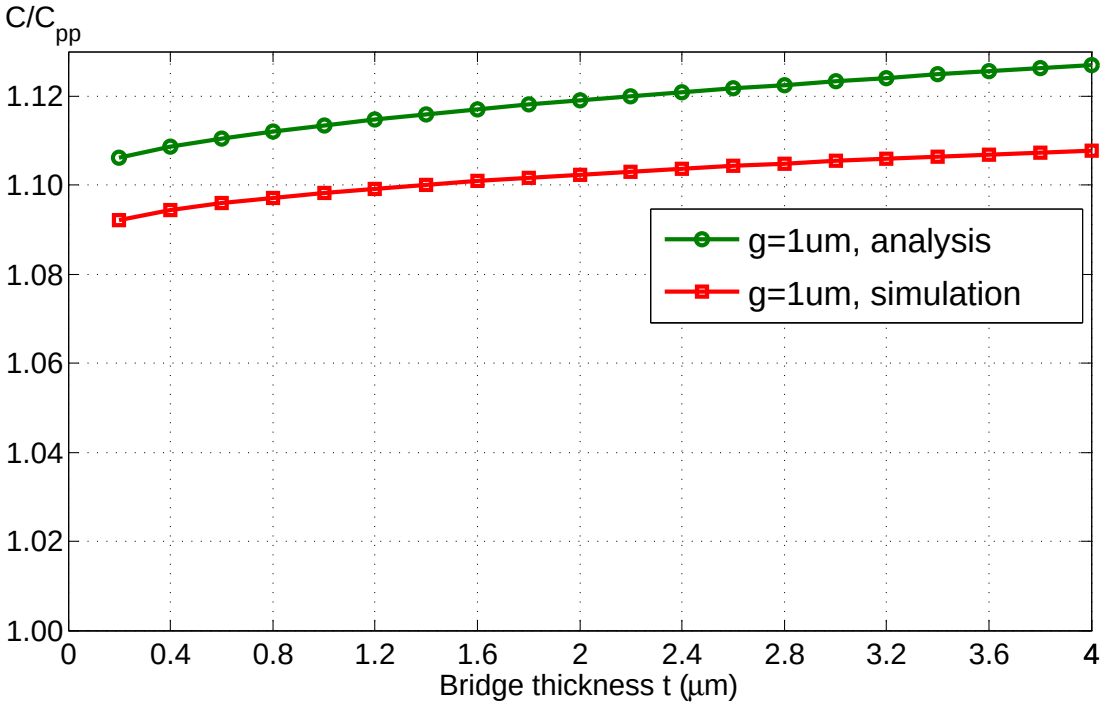

FIGURE 4.1: Relative capacitance as a function of bridge thickness

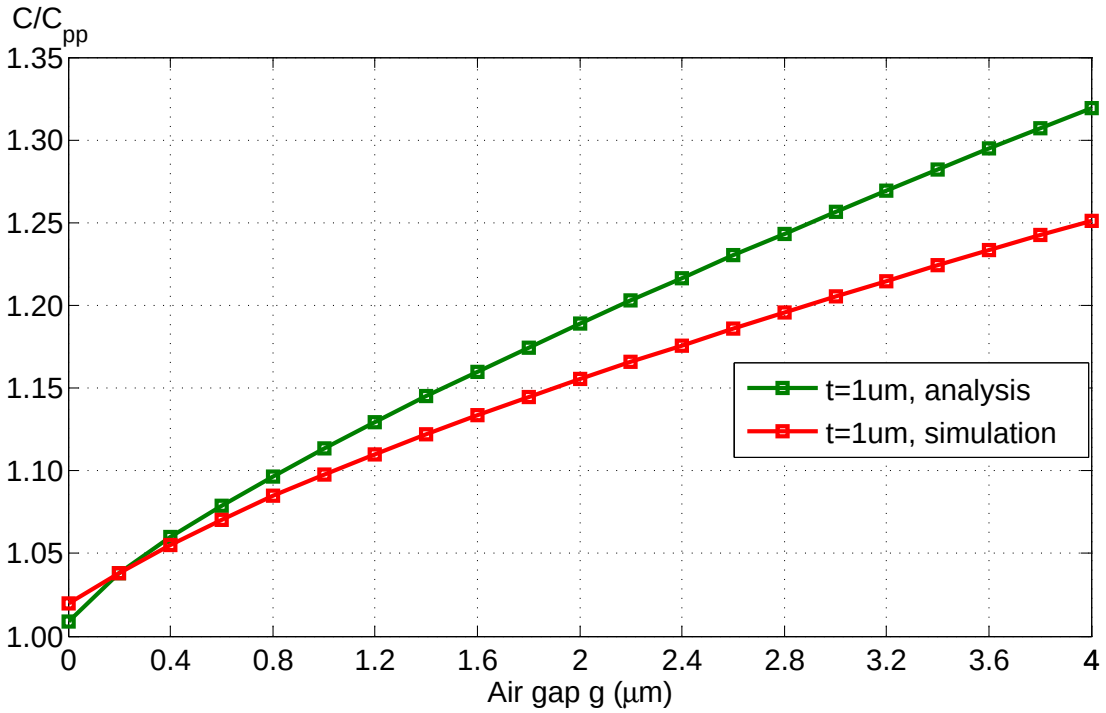

FIGURE 4.2: Relative capacitance as a function of air gap

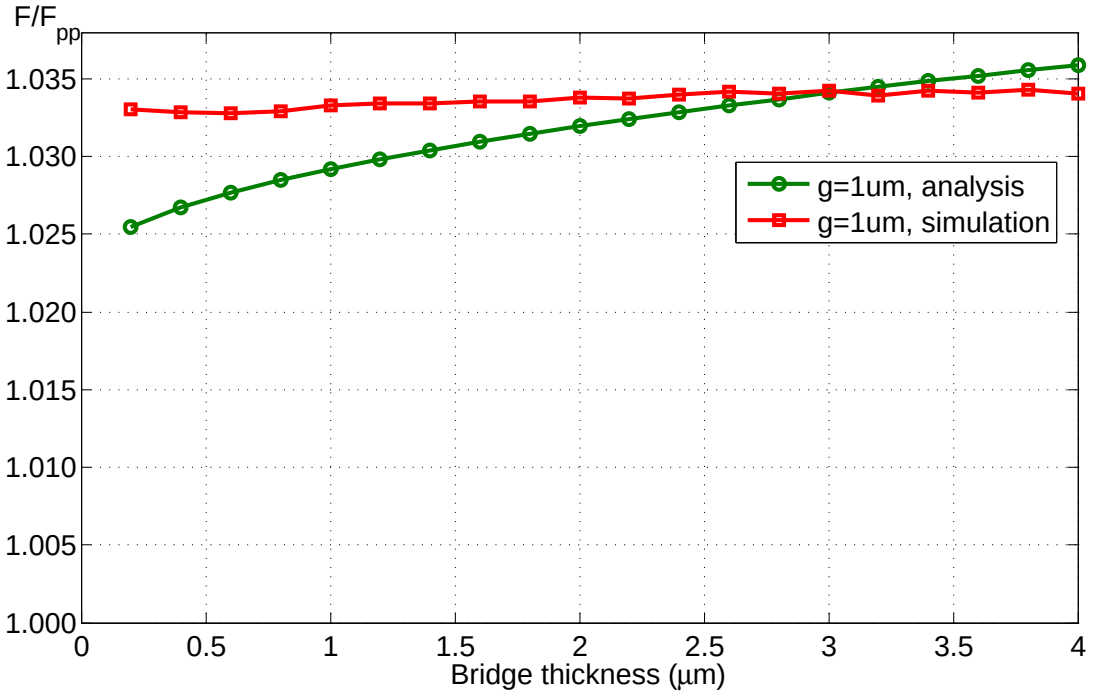

FIGURE 4.3: Relative force as a function of bridge thickness

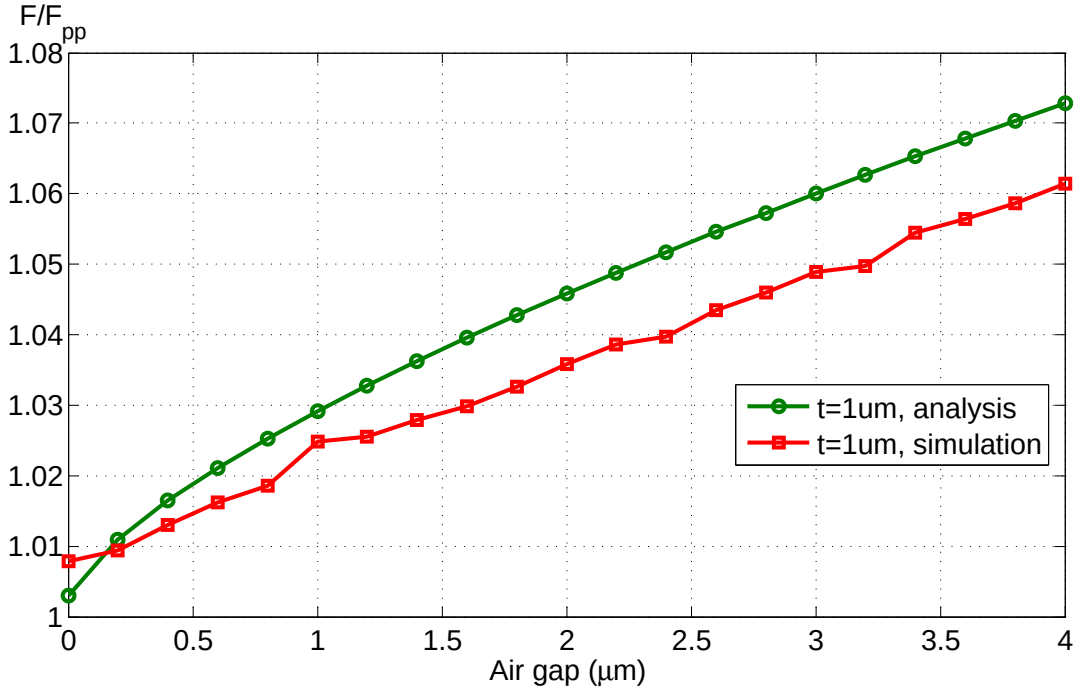

FIGURE 4.4: Relative force as a function of air gap

4.1.2 Derivation of spring constant component due to bending

A Matlab program is written to implement the procedure described in Section 3.1.2, the code is presented in Appendix A.1. With the polynomial P obtained from the program,

the deflection w of the bridge can be calculated at a certain point. For example, the deflection of a switch having $l = 280\ \mu m$, $b = 80\ \mu m$, $t = 1\ \mu m$, $g = 2\ \mu m$, $W = 100\ \mu m$, under a pressure $q = 380\ N/m$ at the central area of $b \times W$ (corresponding to an actuation voltage of $12\ V$) is plotted as a function of coordinate X, Y in Figure 4.5.

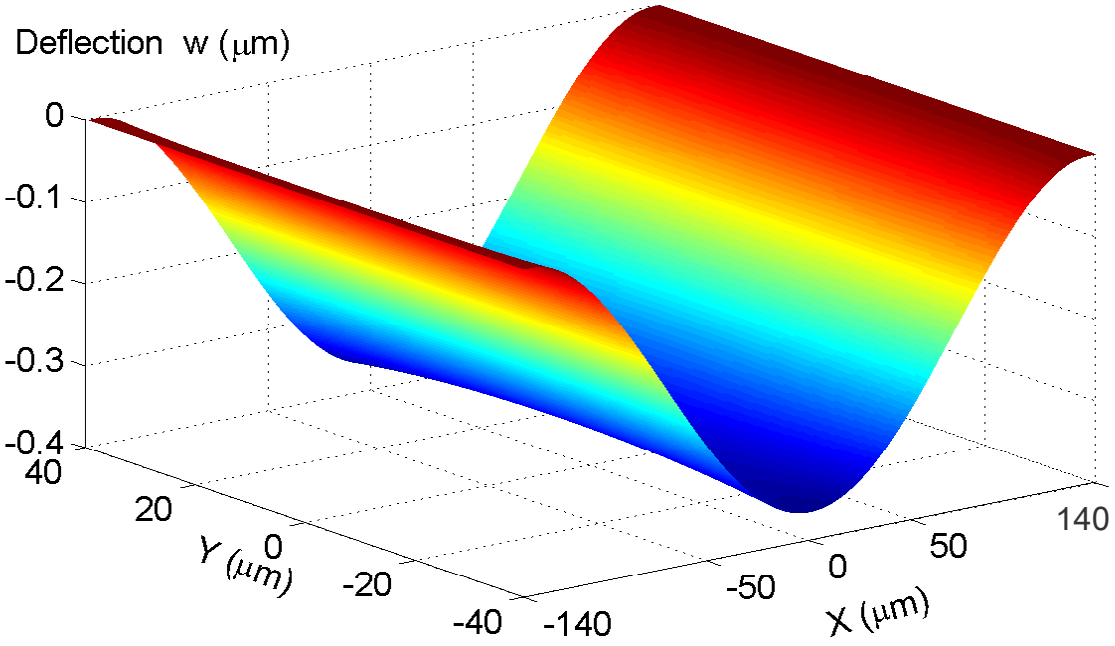

FIGURE 4.5: Deflection w plotted as a function of coordinate X, Y in pure bending

The deflection at the central point of the bridge can now be expressed as a function of mechanical parameters, bridge dimensions and a constant C_b:

$$P(0,0) = C_b \times \frac{24\left(1-\nu^2\right) ql^4}{Et^4} \tag{4.1}$$

Here, C_b is a constant dependent on the Poisson ratio, ν, and the ratios b/l, W/l. Table 4.1 lists values of C_b with various parameter combinations. Knowing C_b, the spring constant of the bridge can be found:

$$k_b = \frac{qbW}{tP(0,0)} = \frac{1}{C_b} \times \frac{EbWt^3}{24\left(1-\nu^2\right) l^4} \tag{4.2}$$

TABLE 4.1: Values of C_b with various parameter combination

$\boldsymbol{\nu}$	$\frac{\mathbf{b}}{\mathbf{l}}$	$\frac{\mathbf{W}}{\mathbf{l}}$	$\mathbf{C_b}$	**Relative error**
0.44 (Gold)	$\frac{40}{280}$	$\frac{100}{280}$	9.59×10^{-4}	0.14%
0.44 (Gold)	$\frac{60}{280}$	$\frac{100}{280}$	9.31×10^{-4}	0.14%
0.44 (Gold)	$\frac{80}{280}$	$\frac{100}{280}$	9.08×10^{-4}	0.11%
0.44 (Gold)	$\frac{80}{280}$	$\frac{80}{280}$	7.54×10^{-4}	0.17%
0.44 (Gold)	$\frac{80}{280}$	$\frac{60}{280}$	5.82×10^{-4}	0.19%

4.1.3 Derivation of spring constant component due to stretching

With the procedure described in Subsection 3.1.3, a Matlab program is developed to calculate the polynomial approximation of displacement u, v and deflection w of the bridge (see Appendix A.2). The deflection at the central point can be expressed as a function of the load q, material properties E, ν, the length l and the thickness t of the bridge:

$$R(0,0) = C_s \times \sqrt[3]{\frac{2(1-\nu^2)ql}{Et}} \tag{4.3}$$

Here, C_s is a constant dependent on the Poisson ratio, ν, and the ratios b/l, W/l. Table 4.2 lists values of C_s with various parameter combinations.

Knowing C_s, the spring constant due to stretching of the bridge can be found:

$$k_s = \frac{qWb}{[tR(0,0)]^3} = \frac{1}{C_s^3} \times \frac{EbtW}{2(1-\nu^2)l^4} \tag{4.4}$$

TABLE 4.2: Values of $C_s$with various parameter combination

$\boldsymbol{\nu}$	$\frac{\mathbf{b}}{\mathbf{l}}$	$\frac{\mathbf{W}}{\mathbf{l}}$	$\mathbf{C_s}$	**Relative error**
0.44 (Gold)	$\frac{60}{280}$	$\frac{100}{280}$	0.269	1.3%
0.44 (Gold)	$\frac{80}{280}$	$\frac{100}{280}$	0.269	1.1%
0.44 (Gold)	$\frac{80}{280}$	$\frac{80}{280}$	0.253	1.6%
0.44 (Gold)	$\frac{80}{280}$	$\frac{60}{280}$	0.233	1.8%

4.1.4 Derivation of spring constant component due to residual stress

A Matlab program is written to implement the procedure described in Subsection 3.1.4, which can be found in Appendix A.3. The deflection at the central point can be expressed as a function of the load q, residual stress T_0, the length l and the thickness t of the bridge

$$R(0,0) = C_r \times \frac{ql}{tT_0} \tag{4.5}$$

where C_r is a constant dependent on the ratios b/l, W/l. Table 4.3 lists values of C_r with various parameter combinations.

Knowing C_r, the spring constant due to axial residual stress can be found:

$$k_r = \frac{1}{C_r} \times \frac{T_0 bWt}{l^2} \tag{4.6}$$

TABLE 4.3: Values of $C_r$with various parameter combination

ν	$\frac{b}{l}$	$\frac{W}{l}$	C_r	Relative error
0.44 (Gold)	$\frac{40}{280}$	$\frac{100}{280}$	7.33×10^{-2}	0.04%
0.44 (Gold)	$\frac{60}{280}$	$\frac{100}{280}$	7.33×10^{-2}	0.04%
0.44 (Gold)	$\frac{80}{280}$	$\frac{100}{280}$	7.33×10^{-2}	0.04%
0.44 (Gold)	$\frac{80}{280}$	$\frac{80}{280}$	6.12×10^{-2}	0.004%
0.44 (Gold)	$\frac{80}{280}$	$\frac{60}{280}$	4.78×10^{-2}	0.06%

4.1.5 Electromechanical analysis of RF MEMS switch

Applying Equation 3.4, 4.2, 3.10, 4.4, 3.24, 4.6 and using values in Table 3.1, 4.1, 4.2, 4.3, the spring constant components due to bending, stretching and residual stress using both 1D analysis and 2D analysis are shown in Table 4.4. The values for perforated bridge are also presented.

The equation of static balanced forces, Equation 3.30, can now be solved using the table of spring constant components, Table 4.4, together with the fringing field effect shown in Figure 4.3 and Figure 4.4. Figure 4.6 shows deflection-voltage curve for a switch of dimensions: $l \times b \times t = 280\mu m \times 80\mu m \times 1\mu m$, bottom electrode width of $W = 100\mu m$ and air gap of $g = 2\mu m$. The analysis result when neglecting stretching effect are also included for comparison. As can be seen on the figure, the pull-in voltage in simulation, 2D analysis, 1D analysis and 2D analysis, neglecting stretching are $15.6V$, $15.3V$, $14.8V$ and $13.3V$ respectively.

TABLE 4.4: Spring constant components with various parameter combinations (the italic, underlined row corresponds to the perforated bridge)

b (μm)	W (μm)	t (μm)	k_{b_1D} (N/m)	k_{b_2D} (N/m)	k_{s_1D} (N/m^3)	k_{s_2D} (N/m^3)	k_{r_1D} (N/m)	k_{r_2D} (N/m)
40	100	0.25	0.04	0.04	3.88E+11	3.63E+11	3.22	3.22
40	100	0.50	0.28	0.31	7.77E+11	7.26E+11	6.43	6.44
40	100	1.00	2.28	2.45	1.55E+12	1.45E+12	12.87	12.88
40	100	2.00	18.24	19.64	3.11E+12	2.90E+12	25.74	25.75
60	100	0.25	0.05	0.06	5.82E+11	5.44E+11	4.83	4.83
60	100	0.50	0.43	0.47	1.16E+12	1.09E+12	9.65	9.66
60	100	1.00	3.42	3.79	2.33E+12	2.18E+12	19.30	19.32
60	100	2.00	27.36	30.34	4.66E+12	4.35E+12	38.61	38.63
80	100	0.25	0.07	0.08	7.77E+11	7.26E+11	6.43	6.44
80	100	0.50	0.57	0.65	1.55E+12	1.45E+12	12.87	12.88
80	100	1.00	4.56	5.18	3.11E+12	2.90E+12	25.74	25.75
80	*100*	*1.00*	*3.47*	*3.82*	*2.36E+12*	*2.19E+12*	*17.50*	*17.51*
80	100	2.00	36.47	41.48	6.21E+12	5.80E+12	51.48	51.51
80	80	0.25	0.07	0.08	7.77E+11	6.98E+11	6.17	6.17
80	80	0.50	0.55	0.62	1.55E+12	1.40E+12	12.33	12.34
80	80	1.00	4.39	4.99	3.11E+12	2.79E+12	24.67	24.68
80	80	2.00	35.11	39.96	6.21E+12	5.58E+12	49.33	49.35
80	60	0.25	0.07	0.08	7.77E+11	6.70E+11	5.92	5.92
80	60	0.50	0.53	0.61	1.55E+12	1.34E+12	11.84	11.85
80	60	1.00	4.26	4.85	3.11E+12	2.68E+12	23.68	23.70
80	60	2.00	34.05	38.83	6.21E+12	5.36E+12	47.36	47.39

FIGURE 4.6: Deflection-voltage curve, given $l \times b \times t = 280\mu m \times 80\mu m \times 1\mu m$, $W = 100\mu m$ and $g = 2\mu m$

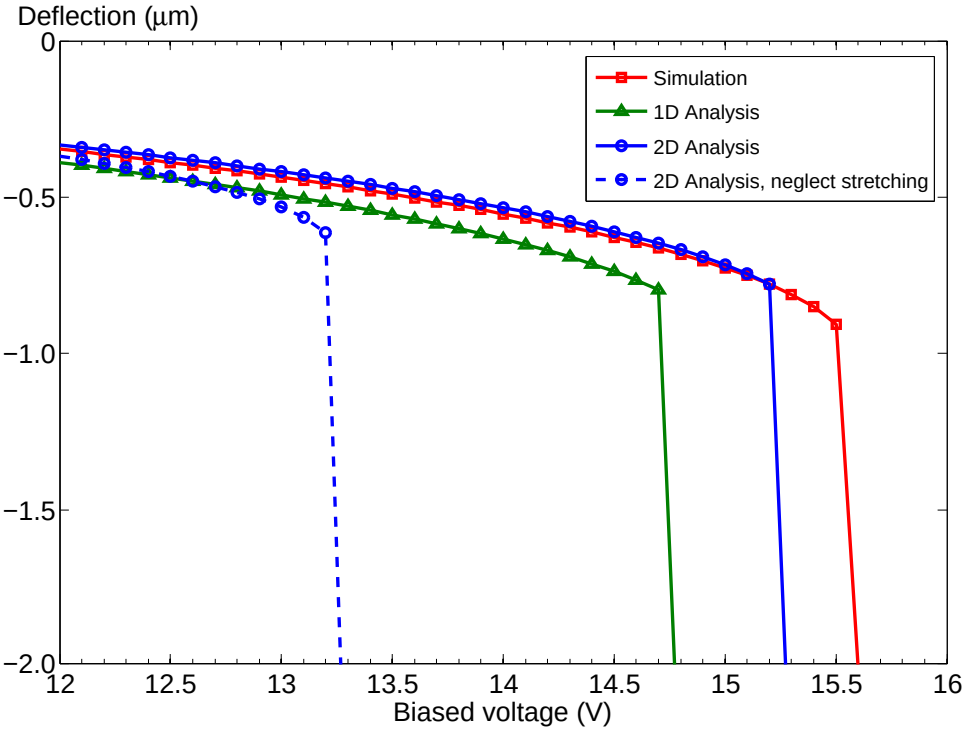

4.1.6 Electromechanical simulation of RF MEMS switch

A. Stationary simulation

In stationary simulation, various values of bridge thickness, air gap and residual tress are studied. The deflection - actuation voltage curve and the pull in voltage are shown in Figure 4.7, Figure 4.8 and Figure 4.9, where in Figure 4.7 the air gap is kept at 2 μm while changing the bridge thickness, in Figure 4.8 the bridge thickness is kept at 2 μm while changing the air gap and in Figure 4.9, the bridge thickness and the air gap are kept at $1\mu m$ and $2\mu m$ respectively while the residual stress is varied.

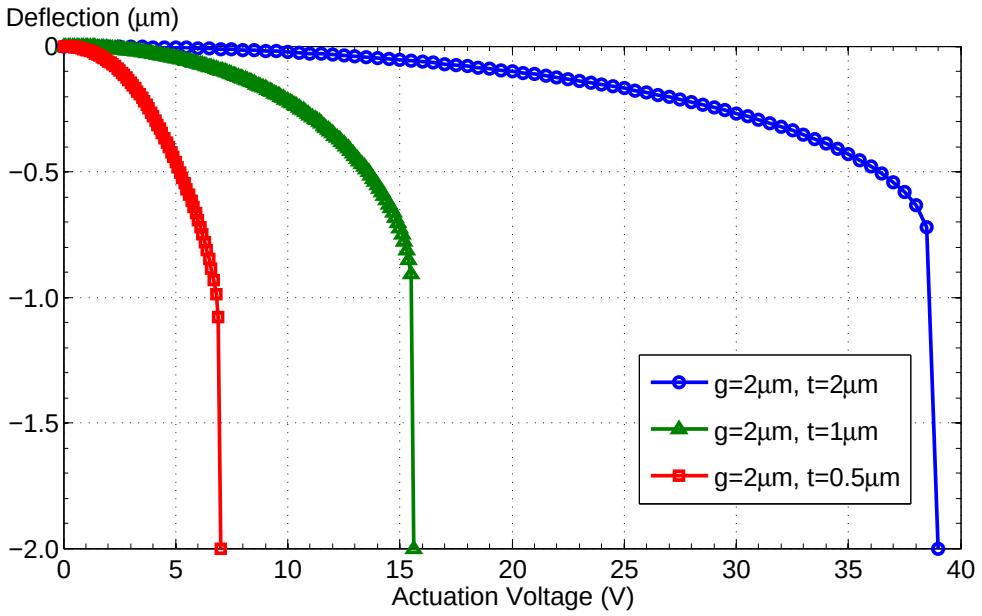

FIGURE 4.7: Deflection-voltage curve with varied bridge thickness

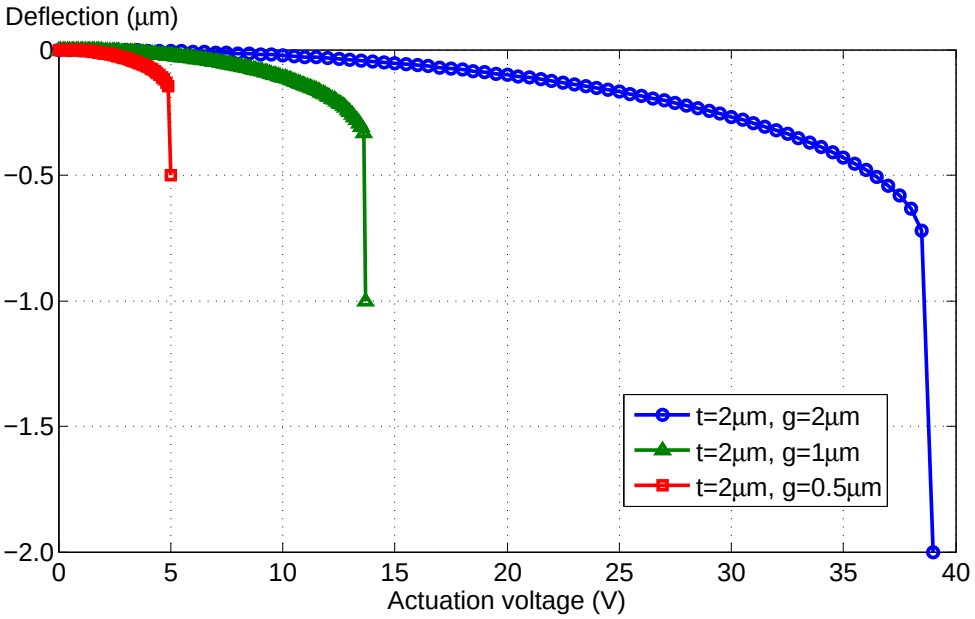

FIGURE 4.8: Deflection-voltage curve with varied air gap

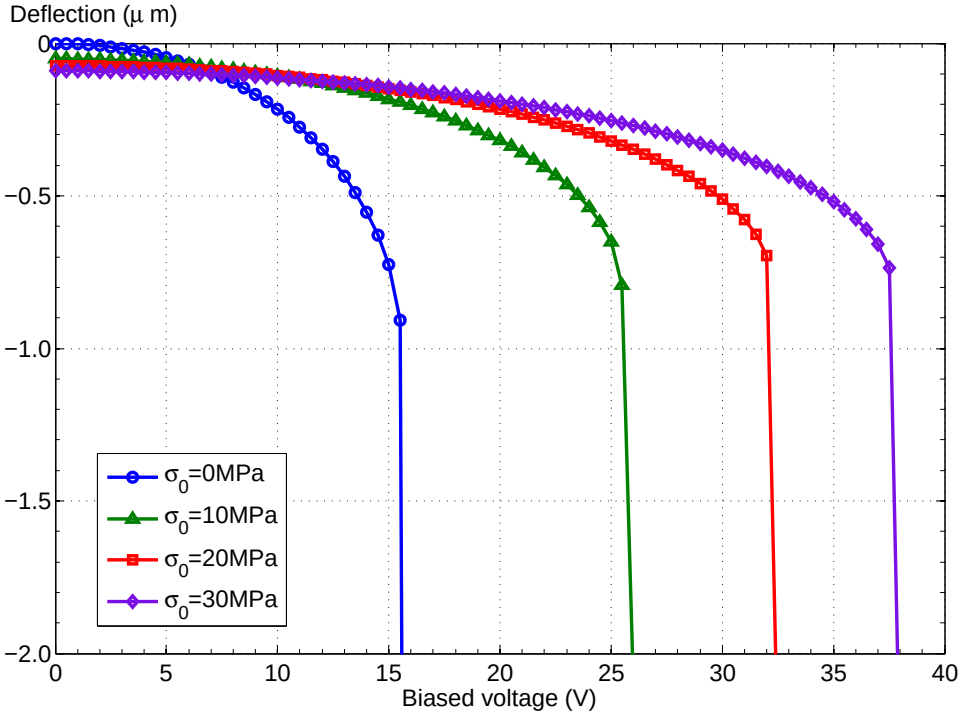

FIGURE 4.9: Deflection-voltage curve with varied axial residual stress

B. Dynamic simulation

The switching time in vacuum and in air are tabulated in Table 4.5, with various combination of bridge thickness, air gap and actuation voltage. The table is divided into four groups where only one parameter is changed in each group.

TABLE 4.5: Switching time of various switches in vaccum and in air

Thickness (µm)	Gap (µm)	$V_{act}/V_{pull\text{-}in}$	Hole	t_{vacuum} (µs)	t_{air} (µs)
0.5	2	1.2	No	17.8	459.7
1	2	1.2	No	7.0	96.0
2	2	1.2	No	8.1	15.2
2	0.5	1.2	No	8.4	502.6
2	1	1.2	No	8.3	89.4
2	2	1.2	No	8.1	15.2
2	2	1	No	11.6	67.7
2	2	1.2	No	8.1	15.2
2	2	1.5	No	5.8	8.4
1	2	1.2	No	7.0	96.0
1	2	1.2	Yes	8.3	8.3

4.2 Electromagnetic analysis and simulation of RF MEMS switch

The insertion loss of a switch in up-state is shown in Figure 4.10. The switch here has dimensions of $l \times b \times t = 280\mu m \times 80\mu m \times 2\mu m$, bottom electrode width of $W = 100\mu m$ and dielectric layer of $t_d = 0.5\mu m$. Since in up-state, the switch can be model as as a shunt capacitance to the ground [11, p. 90], the conductor loss of gold and the conductivity of CuO is neglected in this simulation.
Figure 4.11 shows the isolation of switches having different CuO thicknesses, from 0.2 μm to 0.3 μm.

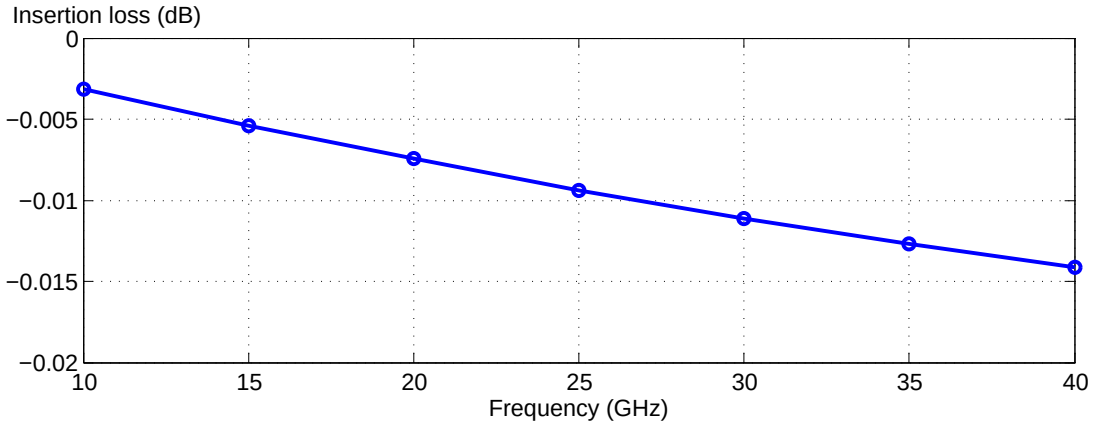

FIGURE 4.10: Insertion loss of a switch in up-state. The switches has dimensions: $l \times b \times t = 280\mu m \times 80\mu m \times 2\mu m$, $W = 100\mu m$ and $t_d = 0.5\mu m$

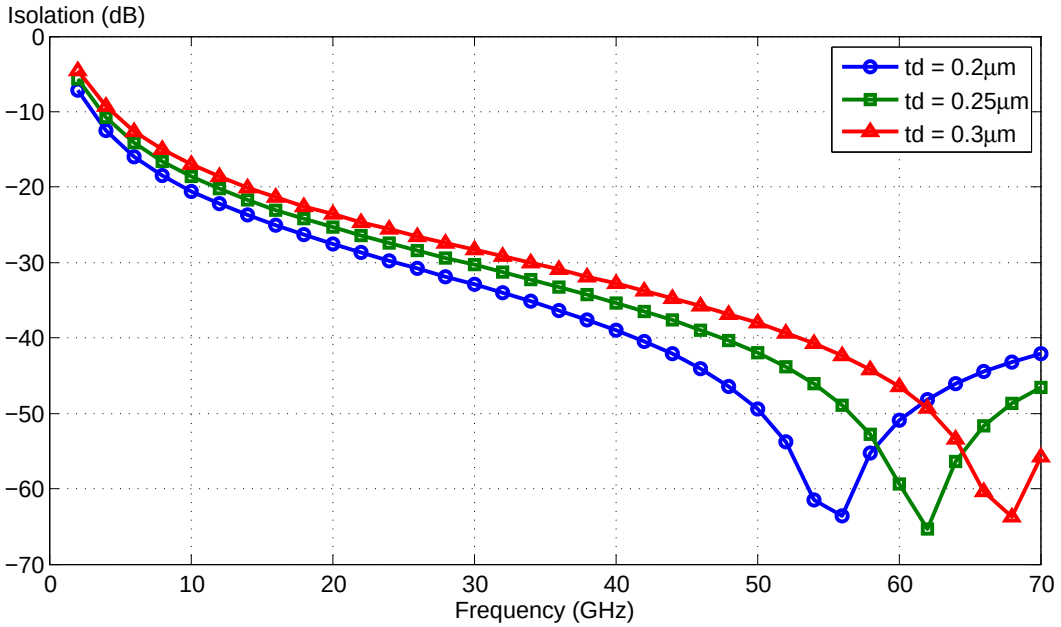

FIGURE 4.11: Isolation up switches in down-state, as a function of CuO dielectric thickness

4.3 Deposition and characterization of Copper(II) oxide

4.3.1 Deposition of Copper (II) Oxide

The surface of oxidized copper films captured by optical microscope are shown in Figure 4.12, together with the experimental conditions.

We calculate the expansion ratio by measuring the sample annealed at 500 °C in 30 minutes since copper is totally oxidized on this sample. The explanation for this will be discussed later in Subsection 5.3.1. The oxide thickness is 730 nm, as measured by stylus profilometer; the expansion ratio is 2.4. Therefore, in order to deposit 300 nm CuO other samples are prepared with the pure copper layer of 125 nm. Figure 4.13 shows the scanned surface of Cu film and CuO film after being annealed for 120 minutes. The average step height is 128 nm and 315 nm for Cu film and CuO film, respectively. The average step height after re-anealing for 60 minutes is 316 nm.

To compare the surface of films annealed with and without air, Figure 4.14 shows the micro image of CuO surface, oxidized at 350 °C for 60 minutes in oxygen (left) and in air (right).

The dendrite structures above CuO surface is scanned and the results are show in Figure 4.15. The height of these structure are around 60 nm

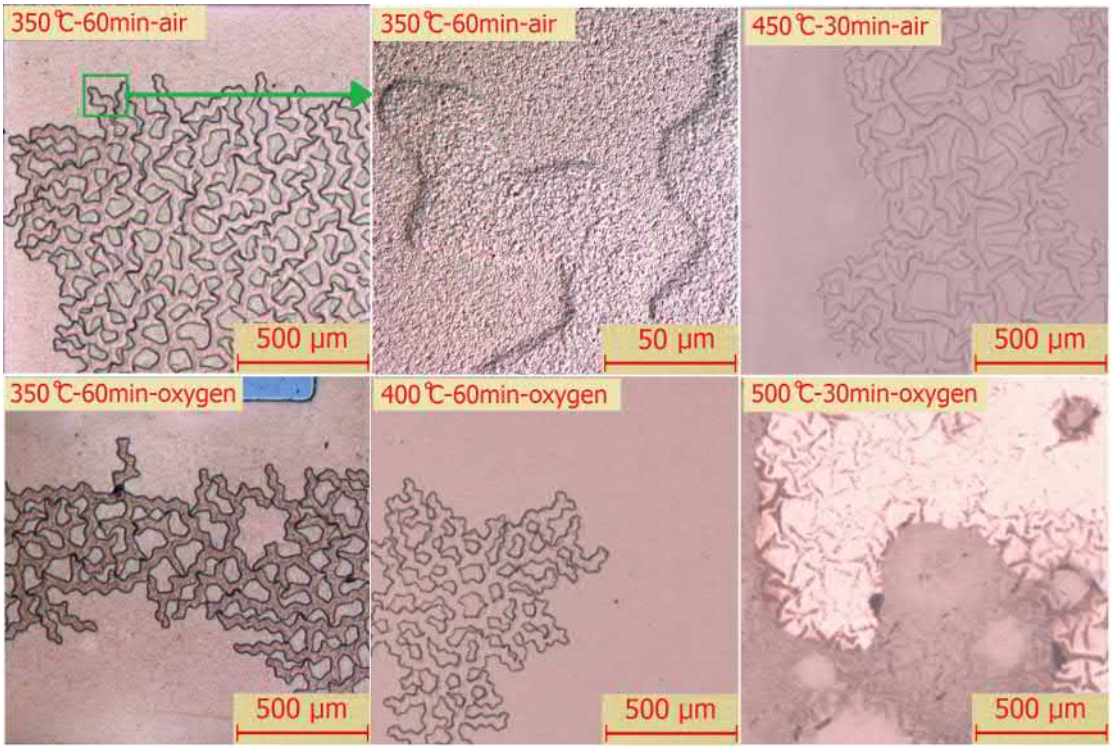

FIGURE 4.12: Surfaces of CuO annealed at various conditions

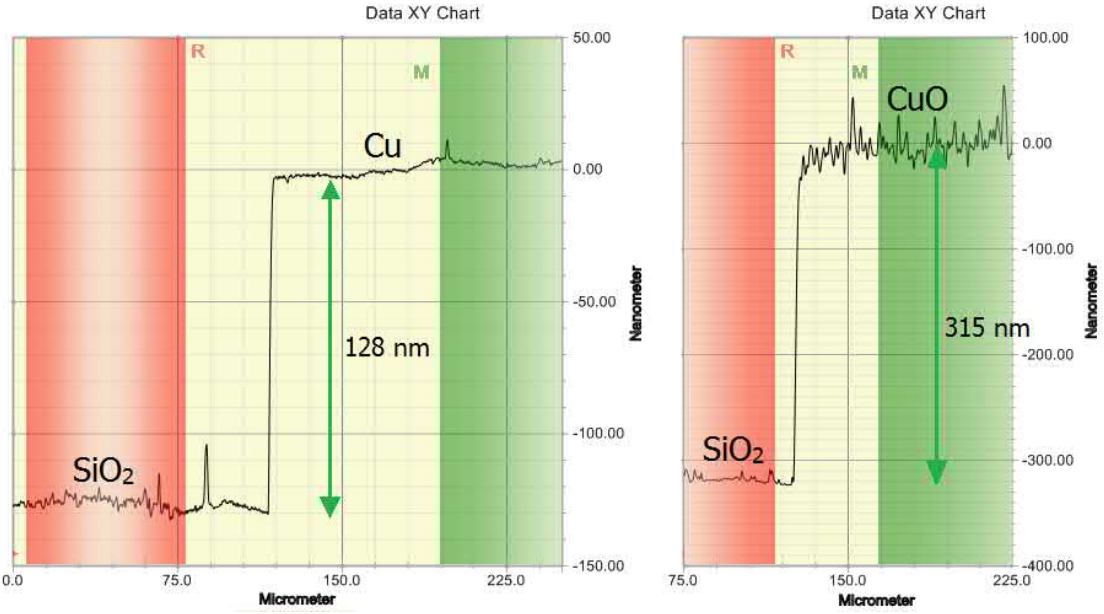

FIGURE 4.13: Stylus scans on Cu/SiO_2 and CuO/SiO_2 films

4.3.2 Measurement of dielectric constant of CuO

The CPWs used for RF measurement have transmission line width: $S = 90\ \mu m$ and CPW gap: $W = 70\ \mu m$. The transmission line length of the sample having CuO and reference sample are 8304 μm and 8331 μm respectively. A small difference in length is due to the placement of the RF GSG probes: they do not stand exactly at the two ends

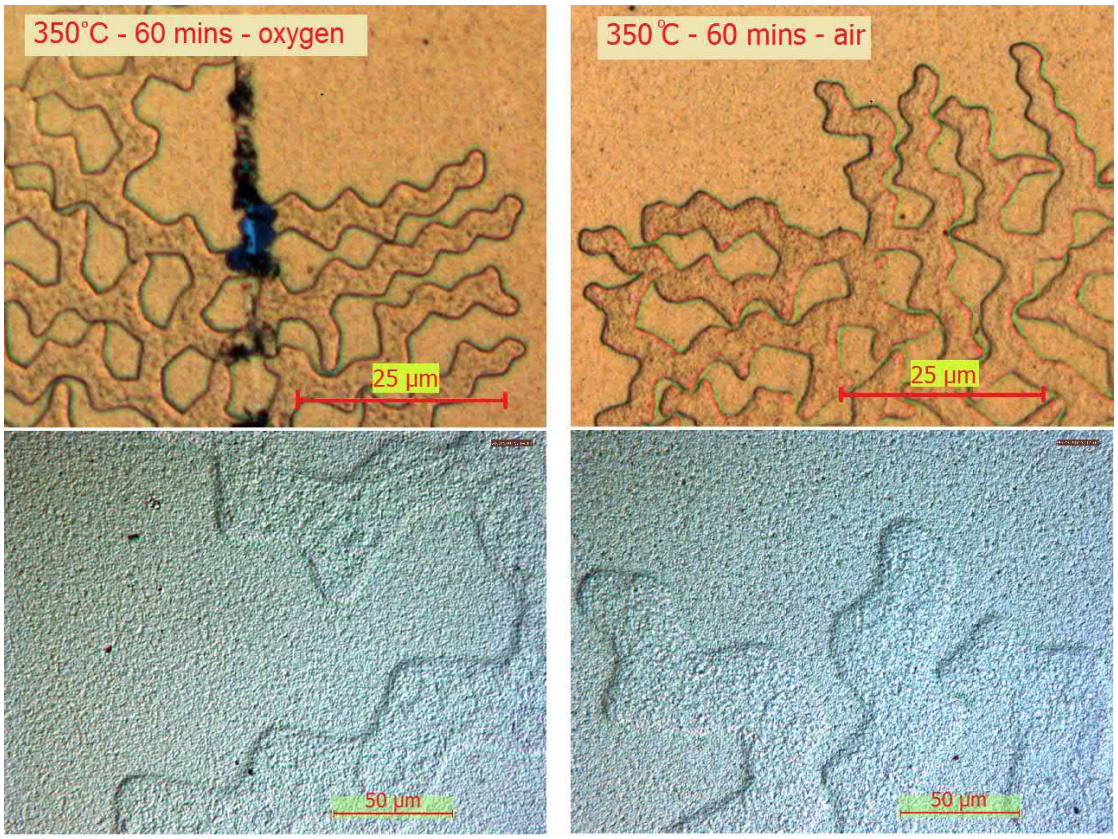

FIGURE 4.14: Surface of CuO annealed in oxygen and in air, at 350 °C for 60 minutes

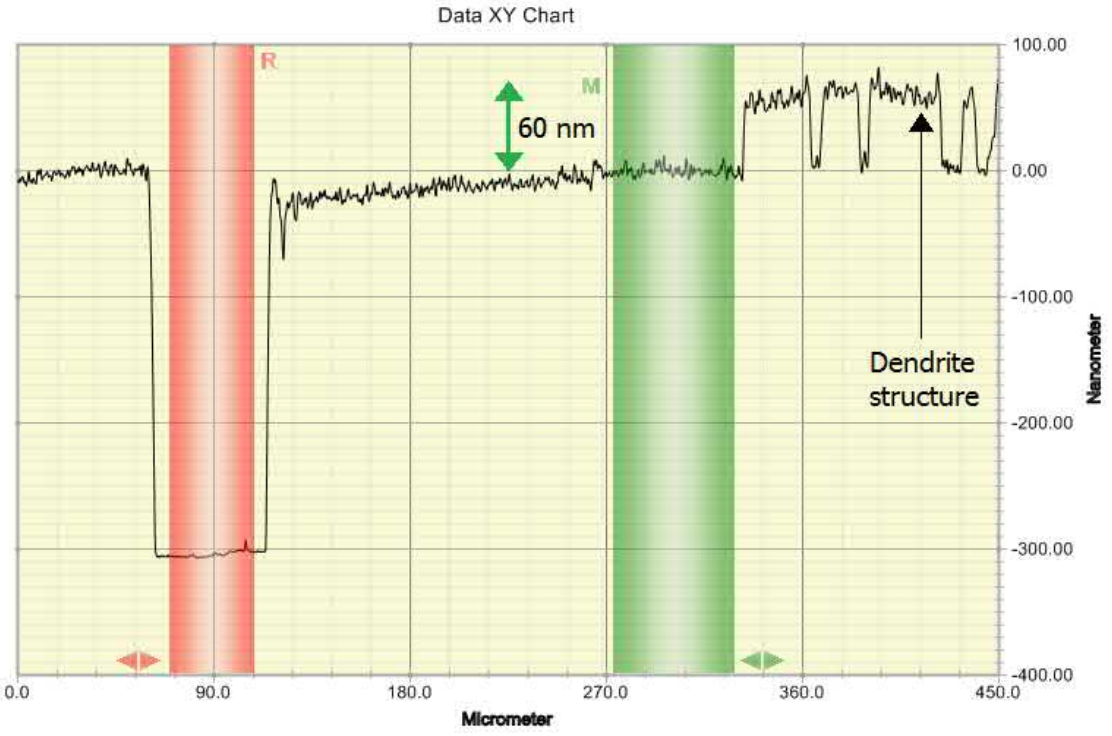

FIGURE 4.15: Height measurement of dendrite structure on CuO surface, annealed in air, at 350 °C

of a CPW. The network analyzer ID is $Rohde\&Schwarz,\ ZVA40-2Port$. Calibration process was done by Deokki, frequency is swept from 100 MHz to 40 GHz with the step of 50 MHz, measured values are averaged 16 times at each frequency value. The phase of S_{21} of the two measured CPWs are shown in Figure 4.16. A Matlab program is written to calculate dielectric constant of CuO, using the two measurement method. The calculated dielectric constant is about -20 over a range from 5 GHz to 40 GHz, which is apparently not correct. The reason for this will be discussed in the Chapter 5.

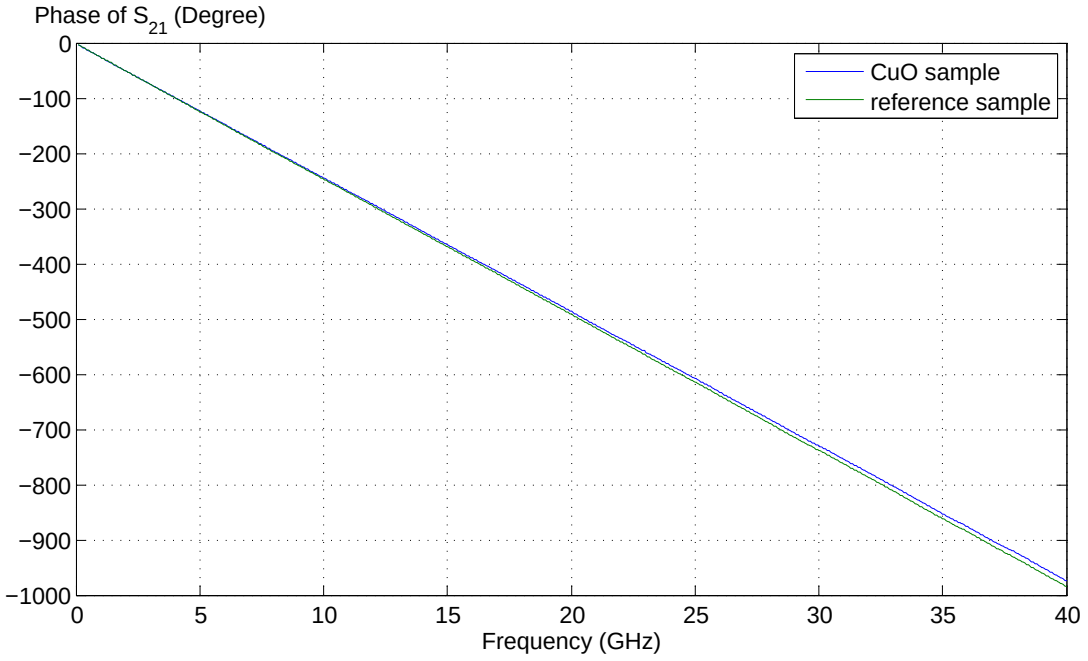

FIGURE 4.16: Phases of S_{21} of the two measured CPWs (with and without CuO layers)

4.3.3 Measurement of dielectric strength of CuO

The oxide film sandwiched between two metal pads is 300 nm, as can be seen in Figure 4.17.

The I-V curves of four MIM capacitors are shown on Figure 4.18. The breakdown voltage are 5.5, 5.8, 5.8 and 6.1 respectively. Therefore, the dielectric strength of CuO is from 0.18 MV/cm to 0.20 MV/cm.

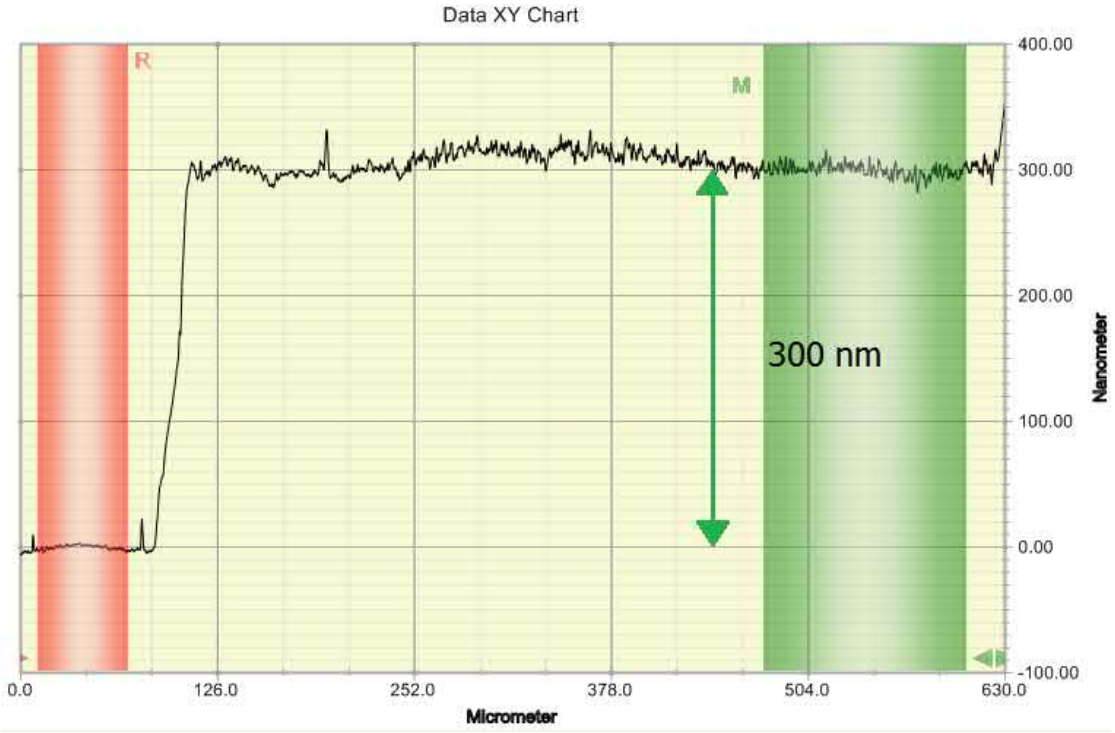

FIGURE 4.17: Thickness of CuO layer of MIM capacitors

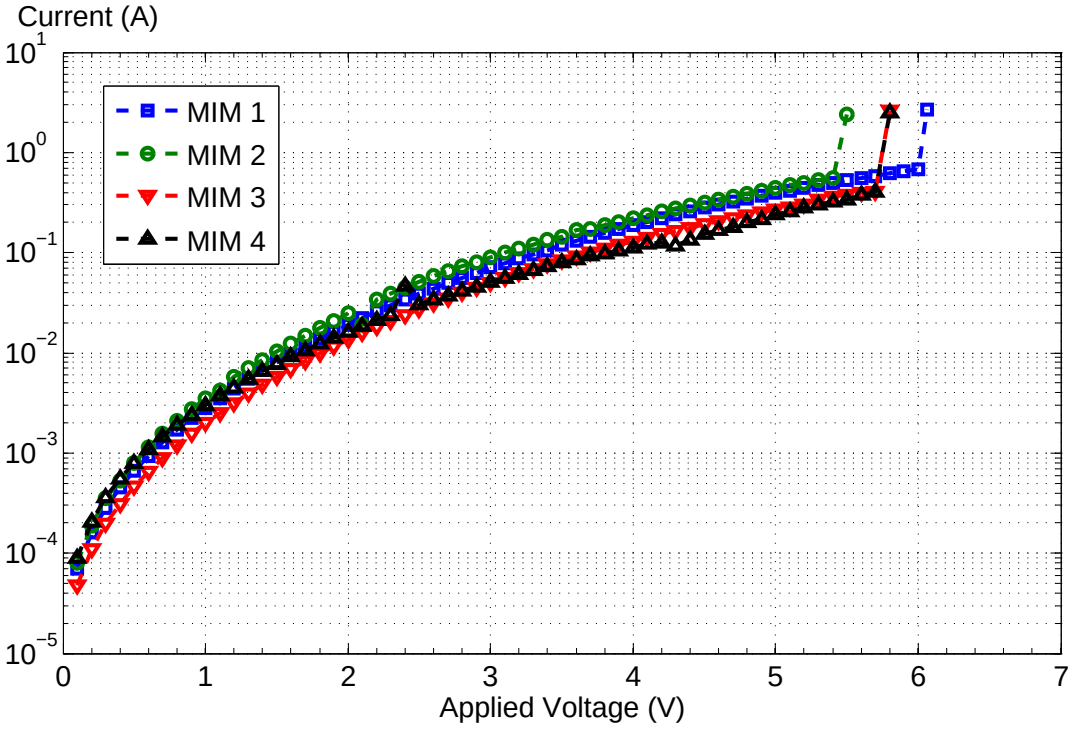

FIGURE 4.18: I-V curves measured on four MIM capacitors which have dielectric thickness of 300 nm and diameters in the $1.1 - 1.4\ mm$ range

Chapter 5

Discussion

5.1 Electromechanical analysis and simulation of RF MEMS switch

5.1.1 Fringing field effect

As can be seen on Figure 4.1 and 4.2, the total capacitance increases slightly with the bridge thickness and quite significant with the air gap. The parallel-plate capacitance is a good approximation for the down-state capacitance but not for the up-state one. For example, for a typical switch having $t = 1\ \mu m$, $g = 2\ \mu m$, the total up-state capacitance is about 115% of the parallel-plate approximation. When comparing the analysis curve and the simulation curve, one can see that the mathematical model for calculating fringing field capacitance presented in Subsection 3.1.1 overestimates the capacitance value by about 4% at the typical gap of $g = 2\ \mu m$. This might be because van de Meijs and Fokkema's assumes an infinite ground plane, which is not the case for the bottom electrode and the bridge and also due to the error of the van de Meijs and Fokkema's formula itself, which is reported to be within 2%.
The curves plotted in Figure 4.3 and 4.4 show that the electrical force when considering fringing effect is not much different from the case when it is neglected, only 3.5% of relative difference for a typical bridge thickness of 1 μm and air gap of 2 μm.
In conclusion, the fringing field effect can be neglected when calculating electrical force and down-state capacitance but should be included when considering up-state capacitance.

5.1.2 Derivation of spring constant components

As can be seen in the plot of deflection w in pure bending using 2D analytical model, Figure 4.5, there is a slight curvature at the middle of the bridge. This is due to the anticlastic effect in a bended plate: when the plate are bended along x axis, the Possion effect gives rise to an opposite curvature along y axis. This shows that the 2D analytical model is able to explore the mechanical properties of the bridge in bending.
The Table of spring constant components, Table 4.4, show good agreement between results of 1D and 2D analysis. There is around 10% of relative difference between k_{b_1D} and k_{b_2D} due to consideration of Poisson's effect in 2D model. For the perforated bridge, it can be seen that the presence of holes lowers the spring constant components by around 20 % $-$ 30 %, due to decrement in effective Young's modulus and release of residual stress to the holes.

5.1.3 Electromechanical analysis of RF MEMS switch

According to the deflection-voltage curves obtained from simulation, 1D analysis and 2D analysis in Figure 4.6, the 2D analysis can approximate well the deflection of the switch comparing with simulation, the pull-in voltage is underestimated by only 2 %. This number for 1D analysis is 5 %. One can also see that neglecting stretching effect could lead to underestimating the pull-in voltage by 15 % for a typical switch ($t = 1\,\mu m,\ g = 2\,mum$).

5.1.4 Electromechanical simulation of RF MEMS switch

A. Stationary simulation
The deflection-voltage curves when changing bridge thickness in Figure 4.7 reveal that the pull-in voltage is lower for thinner bridge, since a thinner bridge is more compliant than a thicker one. One can also see that a thin bridge would snap down at a deflection large than $g/3$ due to stretching. When the bridge thickness is kep constant (Figure 4.8), the smaller air gap, the lower pull-in voltage is. This is because the electrostatic force increases when decreasing the air gap.
It is seen in Figure 4.9 that the pull-in voltage is strongly dependent on the residual stress in several tens MPa range. For example, with a typical switch ($t = 1\,\mu m,\ g = 2\,mum$), a stress of 20 MPa would double the pull-in voltage. Residual stress is rather difficult to control in fabrication of RF MEMS switch. It is a process-dependent parameter and may range from a low compressive stress [3] to a tensile stress of 10-40 MPa [11]. Deokki has also encountered residual stress during making his switches [10]. It

is reported that the fabricated switches are bended down at the center while the pull-in voltage is significantly increased. This may be because of both stress gradient and residual stress: stress gradient would cause deflection at the center while tensile residual stress is the reason why pull-in voltage is higher than expected.

5.2 Electromagnetic analysis and simulation of RF MEMS switch

Figure 4.10 shows that the insertion loss of the simulated switch is satisfied the condition for a well-design switch which requires that the insertion loss should be less than (in magnitude) -0.1 dB. The simulated dielectric thickness here is 0.5 μm; however, since up-state capacitance is nearly independent on the dielectric thickness, this result can be applied for a thinner dielectric layer as well.
In Figure 4.11, one can see that the isolation of the simulated switches also satisfies the posed condition for a well-designed switch: isolation is at least $-20\ dB$ in the targeted range (K_a band, from 27.5 to 40 GHz). It should be noted that the results obtained here are applied for ideal conditions; in real situation, more conditions should be taken into account. For example, the roughness of the CuO layer could significantly lower the down-state capacitance and thus, considerably degrade the "nice" isolation simulated above.

5.3 Deposition and characterization of Copper (II) Oxide

5.3.1 Deposition of Copper (II) Oxide

Figure 4.12 shows that on CuO surface, besides the smooth regions, there appear dendrite structures that grow above the smooth regions. This can be explained by the grained nature of CuO. As has been discussed by [25], at 250 °C CuO begins to nucleate and the crystalline size increases with temperature. The increment in grain size and crystallization leads to compressive stress in the oxide film, creating the dendrite structures that emerge on top of the film. At 450 °C, these structure grows bigger and covers a large surface. At 500 °C, the surface is rough, delaminated and lots of cracks and damages appear. This shows that the metal film has been totally oxidized and stress at the interface CuO/Cr makes the film loses adhesion and peels off.
Figure 4.13 confirms the expansion ratio of 2.4 calculated before. It can be seen that the oxide surface is much rougher than the metal surface due to stress and crystallization. The temperature of 350 °C is the optimized value since as discussed above, the lower

temperature, the lower film stress is and 350 °C is a "safe lower bound" to get rid of Cu_2O [29] [25]. The appropriate annealing time is 120 minutes since re-annealing for one hour would increase the film thickness of only 1 nm, which could be resulted by the measurement noise.
From Figure 4.14, one can see that the oxide surfaces are identical in both cases, meaning that oxygen flow would contribute little effect on annealing process. This confirm that fact that oxygen concentration in atmospheric pressure is abundant for oxidation reaction to happen. Figure 4.15 shows that besides surface roughness, the dendrite structure of height about 60 nm could also hinder the possibility of utilizing CuO as a dielectric material for capacitive RF MEMS switch.

5.3.2 Measurement of dielectric constant of CuO

There are several possible reasons for the wrong value of CuO (around -20). First, as can be seen on Figure 5.1, when the GSG probe is pressed on an end of the CPW on CuO to obtain good contact, the copper layer is peeled off and also, the CuO layer is damaged, causing contact between the probe and underneath Si wafer. This fact show that the adhesion between Cu/CuO and CuO/Si interfaces are not good. This may be due to the stress caused by crystallization of CuO as discussed before and also due to the surface roughness, the dendrite structures on CuO. The second reason, which is less likely to happen, is error in measuring transmission line length. For the designed CPW dimensions, a change in transmission line length of about 1 % could lead to a change in dielectric constant value from -20 to 12, which is rather significant. This problem can be solved by changing the dimensions of CPW: the transmission line length and width, the CPW gap and thickness of the dielectric layer.

5.3.3 Measurement of dielectric strength of CuO

It can be seen from the I-V curves in Figure 4.18 that CuO is a semiconductor, with the resistivity of about 11 $k\Omega cm$ at 4 V. This fact on one hand may increase loss due to resistive heating which is unwanted but on the other hand, as Prof. Ulrik Hanke suggests, could help solve the charging problem usually encountered in dielectrics, such as SiO_2. In these materials, the trapped charges inside dielectrics could increase the pull-in voltage or make MEMS switches lie permanently on dielectric layer. If the dielectric can conduct a little current, like CuO, the trapped charges can follow the current and be released. The low dielectric strength of thermal oxidized CuO (0.2 MV/cm) could hinder the possibility of using it as a dielectric material for MEMS switch. However,

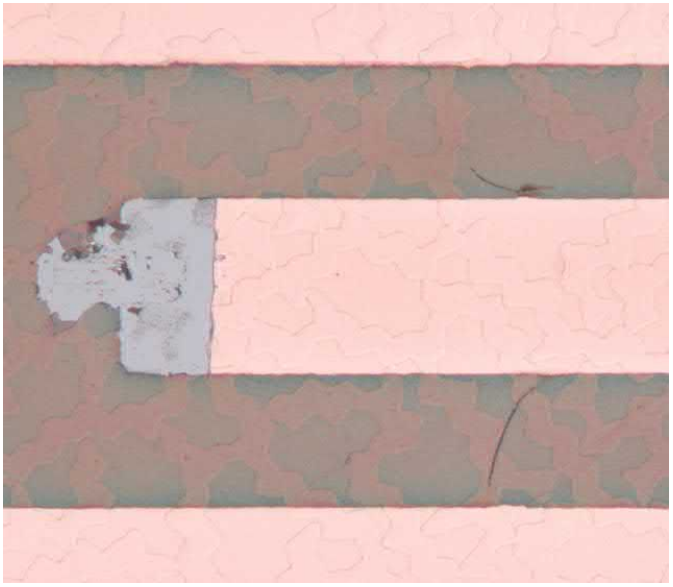

FIGURE 5.1: One end of the CPW on CuO

this problem can be solved by decreasing the stiffness of switch bridge or decreasing the air gap, as discussed in Subsection 5.1.4, so as to lower the required actuation voltage.

Chapter 6

Conclusion

6.1 Designing of RF MEMS switch using CuO dielectric

Now at this point we can look back to our results to discuss a possible design of a CuO switch. Since CuO has a high-k value, it is easy for the switch to possess a high isolation value. However, the difficulty lies in the small dielectric strength of CuO. With a 300 nm thick CuO layer, we may decide the pull-in voltage of $5V$ (and should not more than that value). Since the high capacitance ratio is desirable, it is better to design a large air gap. Thus the thickness of the switch bridge should be small to have a low actuation voltage. For a gold bridge, we could choose the gap to be 2 μm and the bridge thickness to be around 0.4 μm to have a relatively low spring constant. All other dimensions can be kept the same as in Deokki design.
However, these calculation are for a stress-free bridge. In cases where residual stress is significant, the pull-in voltage may now increase to $10-20V$, which is quite large for the annealed CuO layer to withstand. Therefore, in order to still use CuO as a dielectric layer, more investigation should be pay on the process parameter, so as to reduce the residual stress to a very low value.

6.2 Contributions

Through this work, there are two main contributions which have been made. Firstly, in theoretical work, a new, 2D mathematical model has been developed to study mechanical deflection and spring constants of the bridge. The 2D analysis can give more precise results than the traditional 1D analysis. Also, a full simulation frame work for RF MEMS switch has been built, makes it possible to study RF MEMS switch in electromechanics and electromagnetism.

Secondly, in experimental work, the dielectric strength of thermally oxidized CuO has been found to be 0.2 MV/cm, which is quite small comparing with traditional dielectric material like silicon oxide or nitride. Investigation on surface of annealed CuO shows that the dendrite structures due to crystallization of CuO are difficult to avoided at almost all annealing temperatures.

6.3 Future work

So far in this thesis, physical techniques are dominantly used to deposit and characterize the CuO film. To make sure that the metal film is totally oxidized, a trial-and-error process with annealing time is presented where the thickness expansion is used to draw conclusion. We assumed that when oxygen atoms is inserted into metal film, they would enlarge the thickness of the film and when there is no more change in thickness, the film has been totally oxidized. This trial-and-error process can be replaced by a chemical analysis like XRD to better determine the stoichiometry of the film.
Beside CuO, as can be seen in the Table 3.4, some other metal oxides, such as Ta_2O_5, are also possible candidates for the dielectric material of RF MEMS switches. The most important factor that should be considered is their dielectric strength, since a large dielectric strength could give more flexibility and ease in designing the switch.
The simulation part in this thesis can be reuse for further study. One possible future work could be studying the packaging of RF MEMS switches, where a package can be applied outside the model built in this thesis. Various parameters, like isolation of RF MEMS switches, can now be compared between the two cases: with and without the package.

Appendix A

Matlab code

A.1 Matlab code to find approximate solution for deflection of a fixed-fixed plate in bending

```
%This file is writen by Bao Dang Ho to use in his master thesis

syms x y a f R P F I l G q0 W P0 z Z
%nu is the poisson ratio of gold
nu = 0.44;
b = 80/280;
W = 100/280;
syms bc1 bc2 bc3 bc4 bc5 bc6 bc7 bc8
m = 28;

%coefficient matrix of the polynomial
a = sym('a', [m+1 m+1]);
%coefficient matrix of the polynomial after solving the boundary conditions
c = sym('c', [m+1 m+1]);
%variational variables
Z = sym('z', [1 m*(m-10)/8]);
tic

%   STEP 1: EXPRESSING THE DEFLECTION SURFACE AS A POLYNOMIAL

%f is the polynomial
f = 0;
for j=1:m+1
    for i=1:m+2-j
        if mod(j,2)==1 && mod(i,2)==1
        f = f + x^(i-1)*y^(j-1)*a(i,j);
        end
    end
end

```

```
%{
    STEP 2: FIND RELATIONSHIP BETWEEN COEFFICIENTS SO THAT THE POLYNOMIAL SATISFY 8
BOUNDARY CONDITIONS AT 4 BOUNDARIES.
%}
%boundary condition at x=-0.5
  bc1 = subs(f, x, -0.5);
  bc2 = subs(diff(f, x),x,-0.5);
%boundary condition at x=0.5
  bc3 = subs(f, x, 0.5);
  bc4 = subs(diff(f, x),x,0.5);
%boundary condition at y=-b/2
  bc5 = subs(diff(f,y,2)+nu*diff(f,x,2), y, -b/2);
  bc6 = subs(diff(f,y,3)+(2-nu)*diff(diff(f,x,2),y), y, -b/2);
%boundary condition at y=b/2
  bc7 = subs(diff(f,y,2)+nu*diff(f,x,2), y, b/2);
  bc8 = subs(diff(f,y,3)+(2-nu)*diff(diff(f,x,2),y), y, b/2);

  equ='';
%equations for boundary condition 1
[A,Y]=coeffs(bc1,y);
for i=1:size(A,2)
        equ=strcat(equ, char(A(i)), ',');
end
%equations for boundary condition 2
[A,Y]=coeffs(bc2,y);
for i=1:size(A,2)
        equ=strcat(equ, char(A(i)), ',');
end
%equations for boundary condition 3
[A,Y]=coeffs(bc3,y);
for i=1:size(A,2)
        equ=strcat(equ, char(A(i)), ',');
end
%equations for boundary condition 4
[A,Y]=coeffs(bc4,y);
for i=1:size(A,2)
        equ=strcat(equ, char(A(i)), ',');
end
%equations for boundary condition 5
[A,X]=coeffs(bc5,x);
for i=1:size(A,2)
        equ=strcat(equ, char(A(i)), ',');
end
%equations for boundary condition 6
[A,X]=coeffs(bc6,x);
for i=1:size(A,2)
        equ=strcat(equ, char(A(i)), ',');
end
%equations for boundary condition 7
[A,X]=coeffs(bc7,x);
for i=1:size(A,2)
        equ=strcat(equ, char(A(i)), ',');
end
%equations for boundary condition 8
[A,X]=coeffs(bc8,x);
```

```
for i=1:size(A,2)
        equ=strcat(equ, char(A(i)));
        if (i~=size(A,2))
            equ=strcat(equ, ',');
        end
end
var ='';
%variable list
for i=1:m+1
    for j=1:m+2-i
        if mod(j,2)==1 && mod(i,2)==1
            var=strcat(var, char(a(i,j)));
            if i==m+1 && j==1
               continue;
            end
            var=strcat(var, ',');
        end
    end
end
S=solve(equ,var)
s='';
%P is the trial polynomial
P = 0;
for i=1:m+1
    for j=1:m+2-i
        if mod(j,2)==1 && mod(i,2)==1
            s = char(a(i,j));
            P = P + S.(s)*x^(i-1)*y^(j-1);
        end
    end
end
%{
    STEP 3: SOLVE THE VARIATIONAL COEFFICENTS USING THE PRINCIPLE OF
MINIMUM POTENTIAL ENERGY
%}
parametrizedVariables = symvar(P);
oldVariableList = '';
newVariableList = '';
for i=1:m*(m-10)/8+1
   s=strcat('z',num2str(i));
   oldVariableList = strcat (oldVariableList, char(parametrizedVariables(i+2)));
   newVariableList = strcat (newVariableList, s);
   if i~=m*(m-10)/8+1
        oldVariableList = strcat(oldVariableList,',');
        newVariableList = strcat(newVariableList,',');
   end
end
oldVariableList    = strcat('{',oldVariableList,'}');
newVariableList    = strcat('{',newVariableList,'}');
P = subs (P, oldVariableList, newVariableList);
P = vpa(P,32);
%F is the term representing the density of elastic potential energy
F = (diff(P,x,2)+diff(P,y,2))^2-2*(1-nu)*(diff(P,x,2)*diff(P,y,2)-(diff(diff(P,x),y))^2);
%G is the term representing the density of force potential energy
G = -P*q0;
```

```
% F=vpa(F,5);
% G=vpa(G,5);
I = int(int(F,x,-0.5,0.5),y,-b/2,b/2)+int(int(G,x,-0.5*W,0.5*W),y,-b/2,b/2);

strDiff = '';
strZ    = '';
strS    = '';
for i=1:m*(m-10)/8+1
   s=strcat('z',num2str(i));
   strDiff=strcat(strDiff,char(diff(I,s)));
   strZ   =strcat(strZ,s);
   strS   =strcat(strS,'S.',s);
   if i~=m*(m-10)/8+1
        strDiff=strcat(strDiff,',');
        strZ   =strcat(strZ,',');
        strS   =strcat(strS,',');
   end
end
S = solve(strDiff, strZ);
for i=1:m*(m-10)/8+1
    s = strcat('z',num2str(i));s
    P=subs(P,sym(s),S.(s));
end
P0 = subs(P,{x,y},{0,0})
coef = subs(P0,q0,1)
toc
```

A.2 Matlab code to find approximate solution for deflection of a fixed-fixed membrane in stretching

```
%This file is writen by Bao Dang Ho to use in his master thesis

syms x y a b c A B C ex ey exy V P Q R F G
syms I J l G q0 P0 z Z
%nu is the poisson ratio of gold
nu = 0.44;
%depth (width) of the membrane
d = 80/280;
W = 100/280;
syms bc1 bc2 bc3 bc4 bc5 bc6
m = 8;

%coefficient matrix of the polynomial P for u
a = sym('a', [m+1 m+1]);
%coefficient matrix of the polynomial Q for v
b = sym('b', [m+1 m+1]);
%coefficient matrix of the polynomial R for w
c = sym('c', [m+1 m+1]);
N = m*(3*m-2)/8; %number of coefficents to solve by principle of minimum
                 %potential energy
```

```
21 tic
22
23 %   STEP 1: EXPRESSING u, v, w AS POLYNOMIALS
24
25 %P is the trial polynomial for u
26 P = 0;
27 for j=1:m+1
28     for i=1:m+2-j
29         if mod(i,2)==0 && mod(j,2)==1
30         P = P + x^(i-1)*y^(j-1)*a(i,j);
31         end
32     end
33 end
34
35 %Q is the trial polynomial for u
36 Q = 0;
37 for j=1:m+1
38     for i=1:m+2-j
39         if mod(i,2)==1 && mod(j,2)==0
40         Q = Q + x^(i-1)*y^(j-1)*b(i,j);
41         end
42     end
43 end
44
45
46 %R is the trial polynomial for w
47 R = 0;
48 for j=1:m+1
49     for i=1:m+2-j
50         if mod(i,2)==1 && mod(j,2)==1
51         R = R + x^(i-1)*y^(j-1)*c(i,j);
52         end
53     end
54 end
55
56 %{
57     STEP 2: FIND RELATIONSHIP BETWEEN COEFFICIENTS SO THAT THE POLYNOMIAL SATISFY 8
58 BOUNDARY CONDITIONS AT 2 BOUNDARIES: x=-0.5 and x=0.5
59 %}
60 %boundary condition for u at x=-0.5
61   bc1 = subs(P, x, -0.5);
62 %boundary condition for v at x=-0.5
63   bc2 = subs(Q, x, -0.5);
64 %boundary condition for w at x=-0.5
65   bc3 = subs(R, x, -0.5);
66   equ='';
67 %equations for boundary condition 1
68 [A,Y]=coeffs(bc1,y);
69 for i=1:size(A,2)
70         equ=strcat(equ, char(A(i)), ',');
71 end
72 %equations for boundary condition 3
73 [B,Y]=coeffs(bc2,y);
74 for i=1:size(B,2)
75         equ=strcat(equ, char(B(i)), ',');
```

```
76  end
77  %equations for boundary condition 5
78  [C,Y]=coeffs(bc3,y);
79  for i=1:size(C,2)
80          equ=strcat(equ, char(C(i)));
81          if (i~=size(C,2))
82              equ=strcat(equ, ',');
83          end
84  end
85
86
87  var ='';
88  %variable list for P
89  for i=1:m+1
90      for j=1:m+2-i
91          if mod(j,2)==1 && mod(i,2)==0
92              var=strcat(var, char(a(i,j)), ',');
93          end
94      end
95  end
96  %variable list for Q
97  for i=1:m+1
98      for j=1:m+2-i
99          if mod(j,2)==0 && mod(i,2)==1
100             var=strcat(var, char(b(i,j)), ',');
101         end
102     end
103 end
104 %variable list for R
105 for i=1:m+1
106     for j=1:m+2-i
107         if mod(j,2)==1 && mod(i,2)==1
108             var=strcat(var, char(c(i,j)));
109             if i==m+1 && j==1
110                continue;
111             end
112             var=strcat(var, ',');
113         end
114     end
115 end
116   S=solve(equ,var);
117 %P, Q, R will now satisfy boundary conditions
118 s='';
119 P = 0;
120 for i=1:m+1
121     for j=1:m+2-i
122         if mod(j,2)==1 && mod(i,2)==0
123             s = char(a(i,j));
124             P = P + S.(s)*x^(i-1)*y^(j-1);
125         end
126     end
127 end
128 Q = 0;
129 for i=1:m+1
130     for j=1:m+2-i
```

```
131         if mod(j,2)==0 && mod(i,2)==1
132             s = char(b(i,j));
133             Q = Q + S.(s)*x^(i-1)*y^(j-1);
134         end
135     end
136 end
137 R = 0;
138 for i=1:m+1
139     for j=1:m+2-i
140         if mod(j,2)==1 && mod(i,2)==1
141             s = char(c(i,j));
142             R = R + S.(s)*x^(i-1)*y^(j-1);
143         end
144     end
145 end
146 %{
147     STEP 3: SOLVE THE VARIATIONAL COEFFICENTS USING THE PRINCIPLE OF
148 MINIMUM POTENTIAL ENERGY
149 %}
150 %First, replacing variable names generated by Matlab by new names: z1, z2,
151 %...
152 parametrizedVariables = symvar(P+Q+R);
153 oldVariableList = '';
154 newVariableList = '';
155 for i=1:N
156    s=strcat('z',num2str(i));
157    oldVariableList = strcat (oldVariableList, ...
158                                char(parametrizedVariables(i+2)));
159    newVariableList = strcat (newVariableList, s);
160    if i~=N
161         oldVariableList = strcat(oldVariableList,',');
162         newVariableList = strcat(newVariableList,',');
163    end
164 end
165 oldVariableList    = strcat('{',oldVariableList,'}');
166 newVariableList    = strcat('{',newVariableList,'}');
167
168 P = subs (P, oldVariableList, newVariableList);
169 Q = subs (Q, oldVariableList, newVariableList);
170 R = subs (R, oldVariableList, newVariableList);
171 %Calculating normal strain and shear strain in x, y direction
172 ex  = diff(P,x)+0.5*(diff(R,x))^2;
173 ey  = diff(Q,y)+0.5*(diff(R,y))^2;
174 exy = diff(P,y)+diff(Q,x)+diff(R,x)*diff(R,y);
175 % P = vpa(P,32);
176 %F is the term representing the density of elastic potential energy
177 F = ex^2 + ey^2 + 2*nu*ex*ey + 0.5*(1-nu)*exy^2;
178 %G is the term representing the density of force potential energy
179 G = -R*q0;
180 % F=vpa(F,5);
181 % G=vpa(G,5);
182 %I is the term representing the total potential energy
183
184 I = int(int(F,x,-0.5,0.5),y,-d/2,d/2)+int(int(G,x,-0.5*W,0.5*W),y,-d/2,d/2);
185 %I = vpa(I,32)
```

```
%{
    Now solve the system of equations of variational variables: dI/dz1 = 0,
dI/dz2 = 0, dI/dz3 = 0, ...
%}
eqnList = cell(1,N);
J = subs(I,q0,1);
for i = 1:N
   s=strcat('z',num2str(i));
   eqnList{1,i} = char(diff(J,s));
   for j = N:-1:1
   s1=strcat('z',num2str(j));
   s2=strcat('z','(',num2str(j),')');
   eqnList{1,i} = strrep(eqnList{1,i},s1,s2);
   end
end

format long e;
u0 = ones(1, N);  % Make a starting guess at the solution
options = optimset('Display','iter', 'TolX', 1e-30,'TolFun',1e-30);
toc
tic
f = @(u)systemSolver(u,eqnList,N);
[u,fval] = fsolve(f,u0,options) % Call solver
toc
tic
for i=1:N
    s = strcat('z',num2str(i));
    P=subs(P,sym(s),u(i));
    Q=subs(Q,sym(s),u(i));
    R=subs(R,sym(s),u(i));
end
    P=P*q0^(2/3);
    Q=Q*q0^(2/3);
    R=R*q0^(1/3);
R0 = subs(R,{x,y},{0,0});
coef = subs(R0,q0,1)

toc
```

A.3 Matlab code to find approximate solution for deflection of a fixed-fixed plate having residual stress

```
%This file is writen by Bao Dang Ho to use in his master thesis

syms x y a b c A B C ex ey exy V P Q R F G
syms I J l G q0 P0 z Z T0
E = 70e9;
%nu is the poisson ratio of gold
nu = 0.44;
%depth (width) of the membrane
```

```
% T0 = 20e6*(1-nu^2)/E;
d = 80/280;
W = 100/280;
syms bc1 bc2 bc3 bc4 bc5 bc6
for m=4:2:20

%coefficient matrix of the polynomial P for u
a = sym('a', [m+1 m+1]);
%coefficient matrix of the polynomial Q for v
b = sym('b', [m+1 m+1]);
%coefficient matrix of the polynomial R for w
c = sym('c', [m+1 m+1]);
N = m*(3*m-2)/8; %number of coefficents to solve by principle of minimum
                 %potential energy
tic

%   STEP 1: EXPRESSING u, v, w AS POLYNOMIALS

%P is the trial polynomial for u
P = 0;
for j=1:m+1
    for i=1:m+2-j
        if mod(i,2)==0 && mod(j,2)==1
        P = P + x^(i-1)*y^(j-1)*a(i,j);
        end
    end
end

%Q is the trial polynomial for u
Q = 0;
for j=1:m+1
    for i=1:m+2-j
        if mod(i,2)==1 && mod(j,2)==0
        Q = Q + x^(i-1)*y^(j-1)*b(i,j);
        end
    end
end


%R is the trial polynomial for w
R = 0;
for j=1:m+1
    for i=1:m+2-j
        if mod(i,2)==1 && mod(j,2)==1
        R = R + x^(i-1)*y^(j-1)*c(i,j);
        end
    end
end

%{
    STEP 2: FIND RELATIONSHIP BETWEEN COEFFICIENTS SO THAT THE POLYNOMIALS
    SATISFY BOUNDARY CONDITIONS AT 2 BOUNDARIES: x=-0.5 and x=0.5
%}
%boundary condition for u at x=-0.5
  bc1 = subs(P, x, -0.5);
```

```
%boundary condition for v at x=-0.5
  bc2 = subs(Q, x, -0.5);
%boundary condition for w at x=-0.5
  bc3 = subs(R, x, -0.5);
  equ='';
%equations for boundary condition 1
[A,Y]=coeffs(bc1,y);
for i=1:size(A,2)
        equ=strcat(equ, char(A(i)), ',');
end
%equations for boundary condition 3
[B,Y]=coeffs(bc2,y);
for i=1:size(B,2)
        equ=strcat(equ, char(B(i)), ',');
end
%equations for boundary condition 5
[C,Y]=coeffs(bc3,y);
for i=1:size(C,2)
        equ=strcat(equ, char(C(i)));
        if (i~=size(C,2))
            equ=strcat(equ, ',');
        end
end


var ='';
%variable list for P
for i=1:m+1
    for j=1:m+2-i
        if mod(j,2)==1 && mod(i,2)==0
            var=strcat(var, char(a(i,j)), ',');
        end
    end
end
%variable list for Q
for i=1:m+1
    for j=1:m+2-i
        if mod(j,2)==0 && mod(i,2)==1
            var=strcat(var, char(b(i,j)), ',');
        end
    end
end
%variable list for R
for i=1:m+1
    for j=1:m+2-i
        if mod(j,2)==1 && mod(i,2)==1
            var=strcat(var, char(c(i,j)));
            if i==m+1 && j==1
               continue;
            end
            var=strcat(var, ',');
        end
    end
end
  S=solve(equ,var);
```

```
%P, Q, R will now satisfy boundary conditions
s='';
P = 0;
for i=1:m+1
    for j=1:m+2-i
        if mod(j,2)==1 && mod(i,2)==0
            s = char(a(i,j));
            P = P + S.(s)*x^(i-1)*y^(j-1);
        end
    end
end
Q = 0;
for i=1:m+1
    for j=1:m+2-i
        if mod(j,2)==0 && mod(i,2)==1
            s = char(b(i,j));
            Q = Q + S.(s)*x^(i-1)*y^(j-1);
        end
    end
end
R = 0;
for i=1:m+1
    for j=1:m+2-i
        if mod(j,2)==1 && mod(i,2)==1
            s = char(c(i,j));
            R = R + S.(s)*x^(i-1)*y^(j-1);
        end
    end
end
%{
    STEP 3: SOLVE THE VARIATIONAL COEFFICENTS USING THE PRINCIPLE OF
MINIMUM POTENTIAL ENERGY
%}
parametrizedVariables = symvar(P+Q+R);
oldVariableList = '';
newVariableList = '';
for i=1:N
   s=strcat('z',num2str(i));
   oldVariableList = strcat (oldVariableList, ...
                             char(parametrizedVariables(i+2)));
   newVariableList = strcat (newVariableList, s);
   if i~=N
        oldVariableList = strcat(oldVariableList,',');
        newVariableList = strcat(newVariableList,',');
   end
end
oldVariableList    = strcat('{',oldVariableList,'}');
newVariableList    = strcat('{',newVariableList,'}');

P = subs (P, oldVariableList, newVariableList);
Q = subs (Q, oldVariableList, newVariableList);
R = subs (R, oldVariableList, newVariableList);
%Calculating normal strain and shear strain in x, y direction
ex  = diff(P,x)+0.5*(diff(R,x))^2;
ey  = diff(Q,y)+0.5*(diff(R,y))^2;
```

```
exy = diff(P,y)+diff(Q,x)+diff(R,x)*diff(R,y);
% P = vpa(P,32);
%F is the term representing the density of elastic potential energy
F = 0.5*T0*ex;
%G is the term representing the density of force potential energy
G = -R*q0;
% F=vpa(F,5);
% G=vpa(G,5);
%I is the term representing the total potential energy

I = int(int(F,x,-0.5,0.5),y,-d/2,d/2)+int(int(G,x,-0.5*W,0.5*W),y,-d/2,d/2);
%I = vpa(I,32)
%{
    Now solve the system of equations of variational variables: dI/dz1 = 0,
dI/dz2 = 0, dI/dz3 = 0, ...
%}
A = sym(zeros (N,N));
B = sym(zeros (N,1));
J = subs (I, T0, 1);
for i = 1:N % N is the number of new coefficients
    s1   = strcat ( 'z', num2str(i)); %z_i
    temp = diff(J, s1);
    for j = 1:N
        s2     = strcat ( 'z', num2str(j)); %z_j
        A(i,j) = diff(temp,s2);
    end
    B(i,1) = -diff(temp, q0);
end
U=A\B;
Z = U';
%Coefficients {z_i} solved, insert back into P, Q, R
for i = 1:N
    s = strcat('z',num2str(i));
    P = subs(P,sym(s),Z(i));
    Q = subs(Q,sym(s),Z(i));
    R = subs(R,sym(s),Z(i));
end
    P=P*q0/T0;
    Q=Q*q0/T0;
    R=R*q0/T0;
R0 = subs(R,{x,y},{0,0})
coef = subs(R0,{q0,T0},{1,1})

toc

end
```

Bibliography

[1] L.E. Larson, R.H. Hackett, M.A. Melendes, and R.F. Lohr. Micromachined microwave actuator (mimac) technology-a new tuning approach for microwave integrated circuits. In *Microwave and Millimeter-Wave Monolithic Circuits Symposium, 1991. Digest of Papers, IEEE 1991*, pages 27–30, 1991. doi: 10.1109/MCS.1991.148080.

[2] C.L. Goldsmith, Z.J. Yao, S. Eshelman, and David Denniston. Performance of low-loss rf mems capacitive switches. *Microwave and Guided Wave Letters, IEEE*, 8(8): 269–271, 1998. ISSN 1051-8207. doi: 10.1109/75.704410.

[3] Jeremy B. Muldavin and G.M. Rebeiz. High-isolation cpw mems shunt switches. 1. modeling. *Microwave Theory and Techniques, IEEE Transactions on*, 48(6): 1045–1052, 2000. ISSN 0018-9480. doi: 10.1109/22.904743.

[4] S.P. Pacheco, L. P B Katehi, and C.T.-C. Nguyen. Design of low actuation voltage rf mems switch. In *Microwave Symposium Digest. 2000 IEEE MTT-S International*, volume 1, pages 165–168 vol.1, 2000. doi: 10.1109/MWSYM.2000.860921.

[5] S. Duffy, Carl Bozler, Steven Rabe, J. Knecht, L. Travis, P. Wyatt, C. Keast, and M. Gouker. Mems microswitches for reconfigurable microwave circuitry. *Microwave and Wireless Components Letters, IEEE*, 11(3):106–108, 2001. ISSN 1531-1309. doi: 10.1109/7260.915617.

[6] Jae Y. Park, G.H. Kim, K.W. Chung, and Jong U. Bu. Electroplated rf mems capacitive switches. In *Micro Electro Mechanical Systems, 2000. MEMS 2000. The Thirteenth Annual International Conference on*, pages 639–644, 2000. doi: 10.1109/MEMSYS.2000.838593.

[7] K.J. Rangra, R. Marcelli, G. Soncini, F. Giacomozzi, B. Margesin, L. Lorenzelli, V. Mulloni, and C. Collini. Micromachined low actuation voltage rf mems capacitive switches, technology and characterization. In *Semiconductor Conference, 2004. CAS 2004 Proceedings. 2004 International*, volume 1, pages –168, 2004. doi: 10.1109/SMICND.2004.1402830.

[8] T. Lisec, C. Huth, and B. Wagner. Dielectric material impact on capacitive rf mems reliability. In *Microwave Conference, 2004. 34th European*, volume 1, pages 73–76, 2004.

[9] A. Ziaei, T. Dean, and Y. Mancuso. Lifetime characterization of capacitive power rf mems switches. In *Microwave Conference, 2005 European*, volume 3, pages 4 pp.–, 2005. doi: 10.1109/EUMC.2005.1610224.

[10] M. Deokki. *High-k dielectric thin films: characterization and application in RF MEMS capacitive switches*. Dissertation, University of Oslo, 2012.

[11] G.M. Rebeiz. *RF MEMS: Theory, Design, and Technology*. Wiley, 2004. ISBN 9780471462880. URL http://books.google.no/books?id=A7728XHtmzAC.

[12] S. Lucyszyn. *Advanced RF MEMS*. The Cambridge RF and Microwave Engineering Series. Cambridge University Press, 2010. ISBN 9780521897716. URL http://books.google.no/books?id=cX1DRGIv_Z0C.

[13] K. Kurokawa. Power waves and the scattering matrix. *Microwave Theory and Techniques, IEEE Transactions on*, 13(2):194 – 202, mar 1965. ISSN 0018-9480. doi: 10.1109/TMTT.1965.1125964.

[14] D.M. Pozar. *Microwave Engineering*. Wiley, 2011. ISBN 9780470631553. URL http://books.google.no/books?id=Zys5YgEACAAJ.

[15] N.P. van der Meijs and J.T. Fokkema. Vlsi circuit reconstruction from mask topology. *Integration, the VLSI Journal*, 2(2):85 – 119, 1984. ISSN 0167-9260. doi: 10.1016/0167-9260(84)90016-6. URL http://www.sciencedirect.com/science/article/pii/0167926084900166.

[16] W. H. Chang. Analytical ic metal-line capacitance formulas (short papers). *Microwave Theory and Techniques, IEEE Transactions on*, 24(9):608–611, Sep. ISSN 0018-9480. doi: 10.1109/TMTT.1976.1128917.

[17] Milan Batista. Uniformly loaded rectangular thin plates with symmetrical boundary conditions. Technical Report arXiv:1001.3016, Jan 2010.

[18] Cui Shuang. Symplectic elasticity approach for exact bending solutions of rectangular thin plates. Master's thesis, City university of Hong Kong, Hong Kong, 2007.

[19] S. Timoshenko and S. Woinowsky-Krieger. *Theory of plates and shells*. Engineering societies monographs. McGraw-Hill, 1959. URL http://books.google.no/books?id=rTQFAAAAMAAJ.

[20] V.L. Rabinovich, R.K. Gupta, and S.D. Senturia. The effect of release-etch holes on the electromechanical behaviour of mems structures. In *Solid State Sensors and Actuators, 1997. TRANSDUCERS '97 Chicago., 1997 International Conference on*, volume 2, pages 1125–1128 vol.2, 1997. doi: 10.1109/SENSOR.1997.635400.

[21] M. Bao and S. Middelhoek. *Micro Mechanical Transducers: Pressure Sensors, Accelerometers and Gyroscopes*. Handbook of Sensors and Actuators. Elsevier Science, 2000. ISBN 9780080524030. URL http://books.google.no/books?id=OwI_xrvrj1kC.

[22] S.D. Senturia. *Microsystem Design*. Springer, 2000. ISBN 9780792372462. URL http://books.google.no/books?id=G3e3NUV9qu4C.

[23] R.E. Collin. *FOUNDATIONS FOR MICROWAVE ENGINEERING, 2ND ED*. Wiley India Pvt. Limited, 2007. ISBN 9788126515288. URL http://books.google.no/books?id=coBpP2SLiZQC.

[24] E. Carlsson and S. Gevorgian. Conformal mapping of the field and charge distributions in multilayered substrate cpws. *Microwave Theory and Techniques, IEEE Transactions on*, 47(8):1544–1552, 1999. ISSN 0018-9480. doi: 10.1109/22.780407.

[25] L. De Los Santos Valladares, D. Hurtado Salinas, A. Bustamante Dominguez, D. Acosta Najarro, S.I. Khondaker, T. Mitrelias, C.H.W. Barnes, J. Albino Aguiar, and Y. Majima. Crystallization and electrical resistivity of cu_2o and cuo obtained by thermal oxidation of cu thin films on sio_2/si substrates. *Thin Solid Films*, 520 (20):6368 – 6374, 2012. ISSN 0040-6090. doi: 10.1016/j.tsf.2012.06.043. URL http://www.sciencedirect.com/science/article/pii/S0040609012007535.

[26] Edward Graper. *Thin film evaporation guide*.

[27] K.F. Young, H.P.R. Frederikse, Journal of physical, and chemical reference data. *Compilation of the Static Dielectric Constant of Inorganic Solids*. American Chemical Society and the American Institute of Physics, 1973. URL http://books.google.no/books?id=tlepHAAACAAJ.

[28] J. McPherson, J. Kim, A. Shanware, H. Mogul, and J. Rodriguez. Proposed universal relationship between dielectric breakdown and dielectric constant. In *Electron Devices Meeting, 2002. IEDM '02. International*, pages 633–636, 2002. doi: 10.1109/IEDM.2002.1175919.

[29] G Papadimitropoulos, N Vourdas, V Em Vamvakas, and D Davazoglou. Deposition and characterization of copper oxide thin films. *Journal of Physics: Conference Series*, 10(1):182, 2005. URL http://stacks.iop.org/1742-6596/10/i=1/a=045.

[30] M. Ouaddari, S. Delprat, F. Vidal, M. Chaker, and Ke Wu. Microwave characterization of ferroelectric thin-film materials. *Microwave Theory and Techniques, IEEE Transactions on*, 53(4):1390–1397, 2005. ISSN 0018-9480. doi: 10.1109/TMTT.2005.845759.

[31] M. Madou. *Fundamentals of microfabrication: The science of miniaturization*. Taylor & Francis Group, 2002. ISBN 9780849308260. URL http://books.google.no/books?id=9bk3gJeQKBYC.